Clays and Clay Minerals (2024), **72**, e8, 1–17
doi:10.1017/cmn.2024.14

Original Paper

Clay and Fe (oxyhydr)oxide mineralogy in the basalt weathering profile in Hainan (southern China): implications for pedogenesis process

Hanlie Hong[1,2], Jiawei Wang[1], Chaowen Wang[3], Chen Liu[1], Thomas J. Algeo[2,4,5], Lulu Zhao[1], Lian Zhou[5], Daqian Zhang[5] and Qian Fang[2]

[1]School of Earth Sciences, China University of Geosciences, Wuhan, Hubei, China; [2]State Key Laboratory of Biogeology and Environmental Geology, China University of Geosciences, Wuhan, China; [3]Gemmological Institute, China University of Geosciences, Wuhan, Hubei, China; [4]Department of Geosciences, University of Cincinnati, Cincinnati, OH, USA and [5]State Key Laboratory of Geological Processes and Mineral Resources, China University of Geosciences, Wuhan, China

Abstract

In order to gain a better understanding of clay and Fe (oxyhydr)oxide minerals formed during pedogenesis of basalts in tropical monsoonal Hainan (southern China), a basalt-derived lateritic soil at Nanyang, Hainan, was investigated comprehensively. The results show that the lateritic regolith consists uniformly of kaolinite and Fe (oxyhydr)oxide minerals, with trace gibbsite only in the AE horizon. Abundant dioctahedral smectite in the basalt bedrock formed due to primary hydrothermal alteration, and transformed to kaolinite rapidly in the highly weathering saprolite horizon. The 'crystallinity' of kaolinite is notably low and its Hinckley index fluctuates along the soil profile, resulting from intense ferrolysis due to fluctuations between wet/dry climate conditions. From the base to the top of the profile, maghemite shows a decreasing trend, whereas magnetite, hematite, and goethite exhibit a slightly increasing trend, indicating that maghemite formed as an initial product of basalt weathering. Formation of Fe (oxyhydr)oxide species in basalt-derived soil is mainly controlled by local environmental conditions such as soil moisture, redox, and acidic conditions; thus, iron mineral-based paleoclimatic proxies could not be used for subtropical to tropical soils. The highly weathered saprolite has a similar δ^{56}Fe value (+0.06‰) to that (+0.07‰) of the parent rock, while the AE to middle E horizons have greater δ^{56}Fe values of +0.12‰ to +0.19‰. Fe isotopic signatures correlate positively with the Fe mass transfer coefficient (R^2=0.77, n=6, ρ<0.05), indicating repetitive weathering and relative accumulation of isotopically heavier Fe in the upper soil horizons, which occurred by reductive dissolution of organic matter under oxic conditions, as reflected by the greater U/Th.

Keywords: basalt; Fe (oxyhydr)oxides; iron isotopes; kaolinite; soil; weathering

(Received: 26 October 2023; revised: 26 January 2024; accepted: 10 April 2024)

Introduction

Soil and regolith formation usually result from chemical weathering of bedrock (Kovács and Czigány, 2017; Wilson et al., 2017; Hilton and West, 2020). Sub-aerial exposure of basalts occurs on a global scale, comprising ~5% of total land area (Dessert et al., 2003), and these are regarded as the most important igneous rock contributing to pedogenesis and globally integrated weathering fluxes (Kardjilov et al., 2006; Ma et al., 2007; Rasmussen et al., 2010; Li et al., 2016; Borker et al., 2019). In particular, chemical weathering of continental basalts contributes significantly to the balance of atmospheric CO_2, and accounts for up to 30% of CO_2 total consumption (Dupré et al., 2003; Brantley et al., 2023; Krause et al., 2023). Basaltic materials consist of rock-forming minerals (such as chain inosilicates, nesosilicates, alkaline feldspars) and glass but usually no phyllosilicates, and neoformed products are derived from crystallization of gels or solutions through weathering of these minerals and glass (Vingiani et al., 2004; Rasmussen et al., 2010; Watanabe et al., 2023). Under tropical climatic conditions, highly weathered basalts generally form a lateritic regolith with a mineral composition dominated by kaolin clays and iron and aluminum oxides, the types and proportions of which depend on factors such as climate, topography, bedrock lithology, and hydrogeology (Caner et al., 2014; Campodonico et al., 2019). In tropical northern Hainan Island, China, soils derived from quartz tholeiitic basalts of a range of ages are dominated by kaolinite and gibbsite with minor 2:1 clay species that develop in the sequence illite, mixed-layered illite/smectite (Ilt-Sme) and illite/vermiculite (Ilt-Vrm), and vermiculite with increasing age (He et al., 2008). However, a recent investigation of soils in this area found that minor smectite was observed in the tholeiitic basalt bedrock, and clay minerals in the soil profile included mainly kaolinite and trace amounts of smectite as well as chlorite, gibbsite, boehmite, and illite (Jiang et al., 2018).

Corresponding author: Hanlie Hong; Email: honghl8311@aliyun.com
Cite this article: Hong H., Wang J., Wang C., Liu C., Algeo T.J., Zhao L., Zhou L., Zhang D., & Fang Q. (2024). Clay and Fe (oxyhydr)oxide mineralogy in the basalt weathering profile in Hainan (southern China): implications for pedogenesis process. *Clays and Clay Minerals* **72**, e8, 1–17. https://doi.org/10.1017/cmn.2024.14

Magnetite (Mag) and maghemite (Mgh) are the main ferromagnetic minerals that contribute to the magnetic susceptibility of soils, while goethite (Gth) and hematite (Hem) are the most abundant antiferromagnetic Fe (oxyhydr)oxide minerals formed during pedogenesis (Van Dam et al., 2008). Because of accumulation and sensitivity to redox potential of iron during pedogenesis, Fe (oxyhydr)oxide minerals are particularly sensitive to document the weathering and soil development processes. Transformations between ferromagnetic minerals and other Fe (oxyhydr)oxide phases during weathering regulate the magnetic susceptibility of soils (Grogan et al., 2003), which can serve as an indicator of soil environmental conditions and pedogenetic processes (Silva et al., 2013; Ayoubi and Adman, 2019). The magnetic property of soils is often influenced by parent materials and climate conditions due to the formation of different Fe (oxyhydr)oxide minerals during weathering (de Jong et al., 1999). Soils developed from basaltic rocks under tropical to subtropical climates produce secondary Fe (oxyhydr)oxides of mainly maghemite and magnetite (Poggere et al., 2018). In subtropical eastern Zhejiang Province, the main pedogenic iron phases are magnetite and/or maghemite in weakly weathered basalt-derived soils, and magnetite, maghemite, and hematite in highly developed soils, the latter indicating a transformation of magnetite (maghemite) to hematite (Lu et al., 2008). In basaltic substrate soils in tropical Hawaii, Fe (oxyhydr) oxide minerals magnetite, maghemite, goethite, and hematite occur widely as neoformed minerals in soils during weathering, and their relative contents depend dominantly on soil development (Van Dam et al., 2008). As illustrated by concentration-dependent magnetic parameters, the highly weathered basalt-derived regolith in tropical Hainan contains dominantly magnetite, maghemite, and hematite (Ouyang et al., 2015). However, in a basalt-derived lateritic profile near the Nanyang soil in Hainan, Fe (oxyhydr)oxide minerals in the soil were found to be hematite and goethite (Qi et al., 2022).

Intense chemical weathering of basalts at low, tropical latitude with a high precipitation rate influences mobility and cycling of elements and associated isotopic fractionation processes significantly in the supergene environment (Fernández-Caliani and Cantano, 2010; Wu et al., 2019; Santos et al., 2021). Iron in soils occurs mainly in Fe (oxyhydr)oxide minerals, primary silicate minerals, and clay minerals, and to a lesser extent as organically bound Fe (Stucki et al., 1988). During weathering, decomposition of primary silicate minerals releases Fe(II), which is rapidly oxidized and subsequently precipitates as poorly crystalline Fe (oxyhydr) oxide minerals. In soil formation, Fe dissolution, transformation, and translocation may involve some abiotic and biotic processes such as oxidative chemical weathering, biogeochemical reactions, and mineral adsorption, with certain processes being dominant in specific soil profiles (Van Breemen and Buurman, 2002; Dauphas et al., 2017). These processes can influence the formation of Fe (oxyhydr)oxide minerals and the Fe-isotope fractionation in soils relative to their parent materials. Therefore, variations in the Fe-isotope signatures of soils can potentially provide information concerning the relationship of pedogenic processes to Fe behavior (Opfergelt et al., 2017). Although Fe isotope studies of soils have been conducted to investigate specific pedogenic processes, few studies have investigated the vertical variations of iron mineral species and Fe isotope composition in a whole soil profile (Wu et al., 2019; Qi et al., 2022).

Depletion of base cations, significant Si loss, Al and Fe accumulation, and acidic soil conditions are common characteristics of laterite developed from weathering of volcanic rocks in subtropical to tropical environments (Perez-Fodich and Derry, 2019). However, the weathering processes of basalt bedrock and, especially, the evolution of clay minerals and Fe (oxyhydr)oxide minerals in basalt-derived soils continue to be the subject of debate due to lack of reliable determination of soil mineral phases (He et al., 2008; Van Dam et al., 2008; Jiang et al., 2018; Qi et al., 2022), which largely hamper better understanding of the pedogenesis process (Grogan et al., 2003; Opfergelt et al., 2017; Orhan and Hüseyin, 2018; Ayoubi and Adman, 2019; Santos et al., 2021). An investigation of soil formation and associated Fe-isotopic fractionation during basalt weathering under tropical conditions is needed for a comprehensive understanding of the evolution of clay and Fe (oxyhydr)oxide phases during pedogenesis. In this study, an analysis of clay and Fe (oxyhydr) oxide phases, geochemistry, and Fe isotopic compositional changes in the lateritic regolith developed on basaltic rocks on the tropical island of Hainan in southern China was carried out. The aims of this study were to: (1) gain new insights into the processes influencing the formation of Fe (oxyhydr)oxide minerals in combination with Fe isotope evidence; and (2) illustrate the evolution of soil minerals during basalt weathering in a tropical monsoonal climate.

Materials and methods

Soil profile and sampling

The landscape of the Wenchang area consists mainly of rolling terrain with an average altitude of ~42 m. The southwestern part of Wenchang is a low-hill platform, with altitudes ranging from 50 to 150 m, while the northeastern region is a relatively flat plain terrace, with altitudes usually <50 m. It has a subtropical to tropical monsoonal climate with contrasting wet (May–October) and dry (November–April) seasons, with a mean annual precipitation of ~1720 mm, a mean temperature of ~24°C, and a humidity range of 34–87%.

The parent rocks of the weathering regolith on Hainan Island are dominantly basalt, granite and granodiorite. Cenozoic basalts are widely distributed in the northern part of the island, being subdivided into five eruptive intervals: (1) Miocene to Pliocene, e. g. Shimengou and Shimacun basalts, (2) early mid-Pleistocene, e. g. Duowen basalt, (3) mid-Pleistocene, e.g. Dongying basalt, (4) late Pleistocene, e.g. Daotang basalt, and (5) Holocene, e.g. Shishan basalt (Fig. 1; Wang et al., 2012).

The bedrock of the present study section is tholeiitic basalt, representing a Pliocene volcanic eruption with a K-Ar age of ~4 Ma (Zhu and Wang, 1989). The subtropical to tropical monsoonal climate with warm temperatures and high precipitation induced strong chemical weathering of these rocks, generating a relatively thick (up to 15 m) weathering regolith of Oxisols in the study area (Huang et al., 2012; Jiang et al., 2018). The vegetation of this area is characterized by tropical coastal plants consisting dominantly of shrubs and herbs. The study section (110° 38′42.5″E; 19°34′46.7″N) crops out at a quarry site in the low-hill platform area at an altitude of 74 m, close to Nanyang town, Wenchang County, in the northeastern part of Hainan Island (Fig. 1), providing access to a 7.7 m thick soil profile overlying unweathered tholeiitic basalt bedrock (Fig. 2).

The topsoil (0–20 cm) is a brown loamy horizon with a porous and loose crumb structure containing abundant organic matter and plant roots. It was not sampled for this study to avoid disturbing agricultural activities. A reddish-brown loam horizon (AE horizon, 20–100 cm) is present under the topsoil, displaying an homogeneous crumb structure and containing minor plant roots. The underlying eluvial horizon (E horizon, 100–520 cm) is a thick

https://doi.org/10.1017/cmn.2024.14 Published online by Cambridge University Press

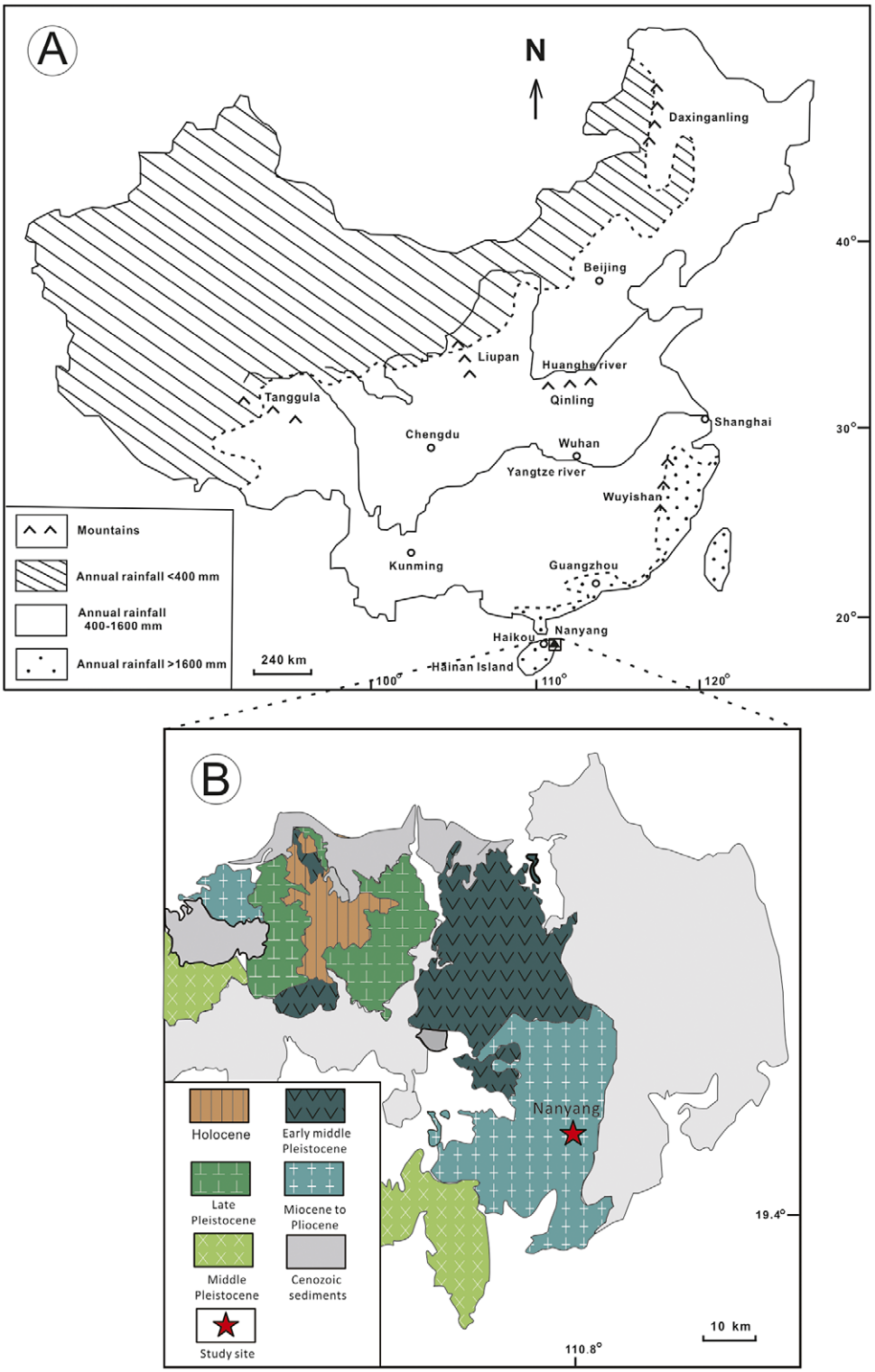

Figure 1. Location and local geology of the study profile. (A) Generalized climate map showing mean annual precipitation in China; (B) regional geological map showing the distribution of basalts of different ages (colors) and Cenozoic sediments (gray) (modified from Wang et al., 2012).

purple red loam horizon that shows a blocky structure and exhibits a distinct mottled texture, having around 20% short white clay veins and spots. The white veins are often incoherent and are significantly fine, with a size of usually <2 cm long and 0.02 mm wide, while the white spots are usually <0.5 cm in size. A light red clayey gravel horizon (B horizon, 520–770 cm) is present beneath the E horizon. It has a banded structure of white clay and red Fe (oxyhydr)oxides, consisting mainly of clays and weathered gravels from the decomposing bedrock, and retains the columnar joint structure of the parent basalt. Close up, the white clay bands exhibit a mottled color due to the presence of large numbers of very fine (<0.1 mm wide) red veins and red spots (<0.2 mm in size), while the red Fe

https://doi.org/10.1017/cmn.2024.14 Published online by Cambridge University Press

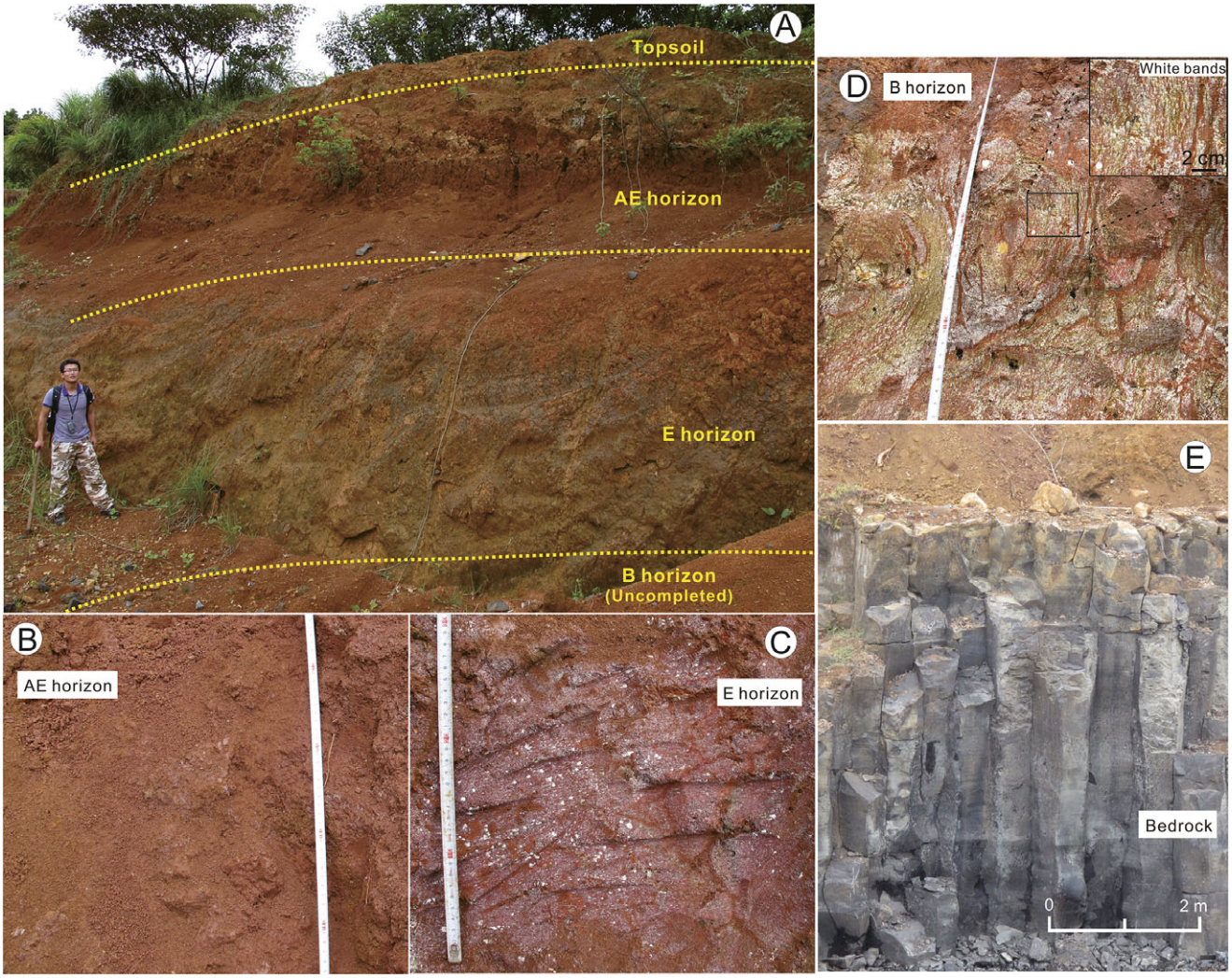

Figure 2. Field photos of the Nanyang weathering soil profile developed on tholeiitic basalt. (A) Full view of the soil profile; (B–E) close-up photographs of the AE, E, and B horizons, and the bedrock, respectively.

(oxyhydr)oxide bands are homogeneously red-brown. The unweathered tholeiitic basalt is grey in color and exhibits an amygdaloidal structure (Fig. 2). Representative samples (~1 kg each) were collected from the weathering profile based mainly on soil horizon and more densely from the eluvial horizon, yielding a total of 11 samples.

Methods

For X-ray diffraction (XRD) analysis, the bulk samples were dried at 60°C in an electric oven overnight, and then ground manually to powder. The mineralogical compositions of the bedrock and the soils were determined for randomly oriented specimens by pressing the powder into a sample holder. The clay fractions extracted from the soils were prepared by pipetting the clay suspension onto glass slides. The XRD measurements were carried out with a Panalytical X'Pert PRO DY2198 (PANalytical Co., Ltd, Eindhoven, Netherlands) diffractometer with Ni-filtered CuKα radiation at a tube voltage of 40 kV and a tube current of 35 mA and a slit system with a 1° divergence slit, a 1° antiscatter slit, and a 0.3 mm receiving slit. The XRD profile was recorded from 3° to 65°2θ at a scan rate of 4°2θ min^{-1} and a step size of 0.02°2θ. The 'crystallinity' of kaolinite was measured using the Hinckley index, which was calculated as the rate of the sum of (1$\bar{1}$0) and (11$\bar{1}$) heights from above a line drawn from the trough between the (020)-(1$\bar{1}$0) peaks to the total height above background of the (1$\bar{1}$0) reflection (Hinckley, 1962; Guggenheim et al., 2002).

For morphological observation of the clay minerals in the soil samples, a small chip (~1 cm in size) of a bulk sample was selected and coated with gold. Scanning electron microscopy (SEM) was performed using an Hitachi SU8010 field emission scanning electron microscope (Hitachi Ltd, Tokyo, Japan) equipped with an Octane Super X-ray energy-dispersive system (EDS) to determine the chemical composition of regions of interest during observation. The SEM instrument was operated at an accelerating voltage of 15 kV and a probe current of 2 nA, with a magnification of up to 8×10^5 and a resolution of 1.0 nm in secondary electron images.

The ^{57}Fe Mössbauer measurements of soil samples were performed at the Key Laboratory for Magnetism and Magnetic Materials of the Ministry of Education of Lanzhou University using in a WSSL-10 Mössbauer spectrometer (Wissel, Germany), which was operated at a temperature of 50K for soil samples and at

https://doi.org/10.1017/cmn.2024.14 Published online by Cambridge University Press

ambient temperature for the basalt bedrock, in transmission mode using a conventional constant acceleration spectrometer and a 25 mCi ^{57}Co source in Rh matrix. Powdered soil samples were packed with lucite powder into Perspex holders. The velocity scale was calibrated by α-Fe foil at ambient temperature. Measurements at 50K were undertaken using a bath cryostat with the sample immersed in nitrogen. The ^{57}Fe Mössbauer spectra were fitted to Lorentzian lines based on the non-linear least-square method, and the Mössbauer parameters were determined using the Moss Winn3.0 program (Waerenborgh et al., 2003). The individual Fe phases in the samples were identified according to their Mössbauer parameters, and the spectral areas of the Fe phases were used to estimate their relative abundances in the samples. The error values of isomer shift and quadrupole splitting were usually ±0.02 mm s^{-1}, and the detection limit was ~1% of the total Fe.

For total organic carbon (TOC) analysis, the soil sample was ground to pass through a 200-mesh sieve using an agate mortar and pestle. The powdered sample was subsequently treated with 0.1 mol L^{-1} hydrochloric acid overnight to remove carbonate impurities. The TOC content was measured on a Vario Macro Cube carbon analyzer (Elementar Analysensysteme GmbH, Hanau, Germany).

X-ray fluorescence (XRF) analysis was used to determine the chemical composition of the soil samples. A loss-on-ignition (LOI) measurement was performed by drying a sample aliquot in an oven at 105°C for 2 h and then heating 1 g of the dried sample to 1000°C for 1.5 h, and the LOI value was then calculated as the weight difference between these sample aliquots. Preparation of fused pellets for XRF measurement was briefly described as follows: the soil sample of 5 g was dried in an electronic oven at 60°C overnight and was subsequently ground to pass through a 200-mesh sieve (particle size <0.074 mm) for further generation of fused XRF pellets. Major element compositions were measured on an XRF-1800 Shimadzu sequential X-ray fluorescence spectrometer (Shimadzu, Tokyo, Japan). In general, the detection limit of major elements was 0.01 wt.%, with a relative standard deviation usually better than 1%.

The gain or loss of each element along the weathering profile was calculated from the mass balance using Th as an immobile reference element, as Th is the least mobile element during basalt weathering under tropical conditions (Brimhall and Dietrich, 1987; Biddle et al., 1998; White and Buss, 2014). The content of a given element in the unaltered bedrock was used as the starting mass, and the mass transfer coefficient of element j relative to the fresh parent rock (τ_{jw}) was calculated as: $\tau_{jw} = (C_{jw}C_{ip})/(C_{jp}C_{iw}) - 1$, where C_{jw} and C_{jp} represent the contents of element j in the weathered soil and the parent rock, respectively, and C_{iw} and C_{ip} represent the concentrations of the immobile reference element i (Th) in the weathered soil and the parent rock, respectively. For element j, τ_{jw} can range from –1 (i.e. complete mobilization) to 0 (i.e. no gain or loss) to +1 (i.e. strong external addition).

Iron isotope ratios were determined by multiple-collector inductively coupled plasma mass spectrometry (Nu Plasma1700 MC-ICP-MS; Nu Instruments, Wrexham, UK). A standard bracketing approach was used to calibrate the machine drift and instrumental mass bias, and a membrane desolvation system (MCN-6000, Cetac Technologies, Omaha, NE) was used to minimize argide interferences (ArN^+, ArO^+, $ArOH^+$) to a background/signal ratio of usually <0.001. Comparison between laboratories was made based on the BHVO-2 standard, which has a δ^{56}Fe value of 0.114±0.011‰ (Craddock and Dauphas, 2011). The ^{57}Fe/^{54}Fe and ^{56}Fe/^{54}Fe ratios were measured simultaneously, and iron isotope compositions were reported in per mille (‰) relative to the average of igneous rocks (Beard et al., 2003), i.e. $\delta^{56}Fe = [(^{56}Fe/^{54}Fe)_{sample}/(^{56}Fe/^{54}Fe)_{igneous} - 1] \times 10^3$. Each sample was measured three times, with the reproducibility (2SD) of these replicate sample measurements shown as an error bar in the figures. The reproducibility of δ^{56}Fe measurements was tested using the BHVO-2 standard after every six samples and at the end of each analytical run.

Results

Clay minerals and Fe (oxyhydr)oxides in the weathering profile

The basalt bedrock consists dominantly of smectite (14.8, 1.54, 1.48 Å), plagioclase (6.45, 4.05, 3.75, 3.64, 3.20, 2.52, 2.13, 1.75 Å), and pyroxene (2.99, 2.52, 1.75, 1.63 Å), with negligible amorphous diffraction backgrounds, suggesting that the glassy component of the basalt bedrock has largely altered into smectite in the supergene environment. Also, the smectite (060) reflection of both 1.54 Å and 1.50 Å indicates the presence of mixed dioctahedral and trioctahedral structures. The weathering profile consists mainly of kaolinite (7.15, 4.47, 3.58, 2.34, 1.49 Å), Fe (oxyhydr)oxides, including hematite (2.70, 1.69 Å), magnetite (2.52, 1.49 Å), maghemite (2.52, 1.47 Å), and goethite (2.70, 4.18 Å). Additionally, the AE horizon contains trace amounts of gibbsite while the lower portion of the B horizon contains trace quartz, as reflected by the characteristic XRD peaks of these minerals (Fig. 3). For the soil samples, kaolinite in the AE horizon and the lower part of the B horizon has generally better 'crystallinity' relative to that from other horizons, based on stronger (001) reflections (Fig. 3).

Under SEM observation, clay flakes in the soil profile exhibit a uniform smooth and flat basal (001) plane and display a generally poorly developed pseudohexagonal morphology with irregular or ragged edges, with significantly small thickness of the edge dimension (Fig. 4). The particle sizes of kaolinite are usually <0.5 μm, suggesting generally less 'crystallinity' (Fig. 4A–C). Occasionally, the clay aggregates show a booklet shape (Fig. 4A), which is typical of kaolinite generated from supergene weathering of feldspars. The EDS analysis showed a chemical composition of dominantly Si, Al, and trace Fe, with a Si/Al ratio of ~0.96 (Fig. 4D), corresponding well to the typical crystal chemical composition of kaolinite. The basalt bedrock shows generally a loose porous structure, with abundant small clay flakes (Fig. 4E). These clay flakes occur in fissures or in the interstitial spaces, and often form on the surfaces and replace residual basalt particles, with a particle size of usually <0.3 μm and typically curled edges and wave-shaped outlines. EDS analysis shows that these clay flakes consist mainly of Si, Al, and minor Mg, Fe, Ca, and Na, with a Si/Al value of 3.83, suggesting the presence of smectitic clays (Fig. 4F).

Mössbauer spectra of the soil samples were fitted to sextets and doublets (Fig. 5), which were derived from an iron-bearing phase or from a set of unresolved contributions of Fe-bearing phases, and the relative area (RA) of each doublet or sextet is proportionally related to the abundance of Fe in the mineral phase (Table 1; Fig. 6). In the spectra of soil samples, a doublet with an isomer shift (IS) of 0.567–0.637 mm s^{-1} and a quadrupole shift (QS) of 0.744–0.850 mm s^{-1} corresponds to Fe^{3+} in silicates (phyllosilicates). Sextets often correspond to microcrystalline Fe (oxyhydr)oxides in the soil samples: those with an IS of

https://doi.org/10.1017/cmn.2024.14 Published online by Cambridge University Press

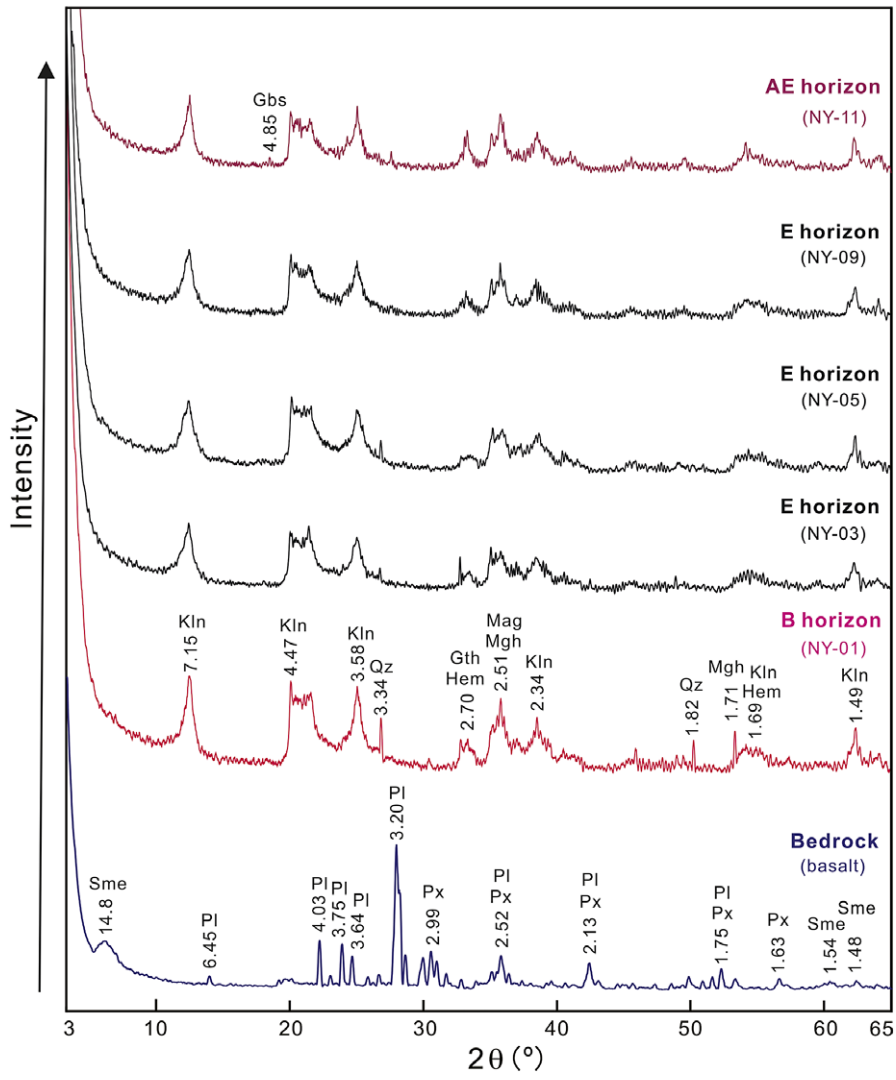

Figure 3. X-ray diffraction patterns of representative samples of the Nanyang soil profile showing mineral compositions by soil horizons. Sme = smectite; Pl = plagioclase; Px = pyroxene; Kln = kaolinite; Qz = quartz; Hem = hematite; Gth = goethite; Mgh = maghemite; Mag = magnetite; Gbs = gibbsite.

0.466–0.552 mm s^{-1} and QS of –0.143 to −0.263 mm s^{-1} are typically hematite; those with IS of 0.450–0.548 mm s^{-1}, QS of –0.085 to −0.261 mm s^{-1}, and a magnetic hyperfine field of 49.71–51.00 T are indicative of goethite; those with IS of 0.449–0.577 mm s^{-1}, QS of –0.123 to –0.365 mm s^{-1}, and a magnetic hyperfine field of 44.80–47.74 T are characteristic of $Fe^{2.5+}$ in magnetite; and those with IS of 0.497–0.650 mm s^{-1}, QS of around 0 to –0.388 mm s^{-1}, and a magnetic hyperfine field of 28.52–38.41 T are maghemite. The Mössbauer spectrum of the basalt bedrock consists of three patterns of doublets (Fig. 5). The doublet with IS of 0.310 mm s^{-1} and QS of 0.886 mm s^{-1} is attributed to Fe^{3+} in silicates (phyllosilicates and pyroxenes), while the doublets with IS of 1.117 mm s^{-1} and QS of 1.963 mm s^{-1} and those with IS of 1.878 mm s^{-1} and QS of 1.105 mm s^{-1} are characteristic of Fe^{2+} in two kinds of silicate phases. The abundance of maghemite decreases gradually from the lower to the upper part of the weathering profile, whereas the contents of hematite, goethite, and magnetite generally exhibit the opposite trend. Iron in the bedrock occurs mainly as Fe^{3+} in phyllosilicates and pyroxenes and Fe^{2+} in two silicate phases in addition to those in magnetite, but Fe^{2+} was not observed in the soil due to intense chemical weathering.

Geochemical and iron isotope compositions of the soil samples

TOC values and geochemical compositions of the soil samples are listed in Table 2. The TOC content of the Nanyang soil is generally low, ranging from 0.10 to 0.27%. Samples from the upper part of the soil profile yield greater TOC values (>0.16%), with the highest value (0.27%) in the AE horizon, whereas samples from the lower part of the profile exhibit smaller and more stable TOC values (0.10–0.13%). The Nanyang soil shows significantly uniform geochemical composition along the weathering profile, with only small differences between samples from different soil horizons (Table 2). The B horizon sample contains more SiO_2 (37.2%) than the AE and E horizon samples (33.5–35.9%). TiO_2 and Fe_2O_3 display similar trends, having uniformly larger values of 3.47–3.88% and 20.9–22.2% in the soil profile, with only slightly smaller values of 3.21–3.39% and 19.2–19.8%, respectively, in the lower E horizon. Al_2O_3 has generally high and uniform values and

https://doi.org/10.1017/cmn.2024.14 Published online by Cambridge University Press

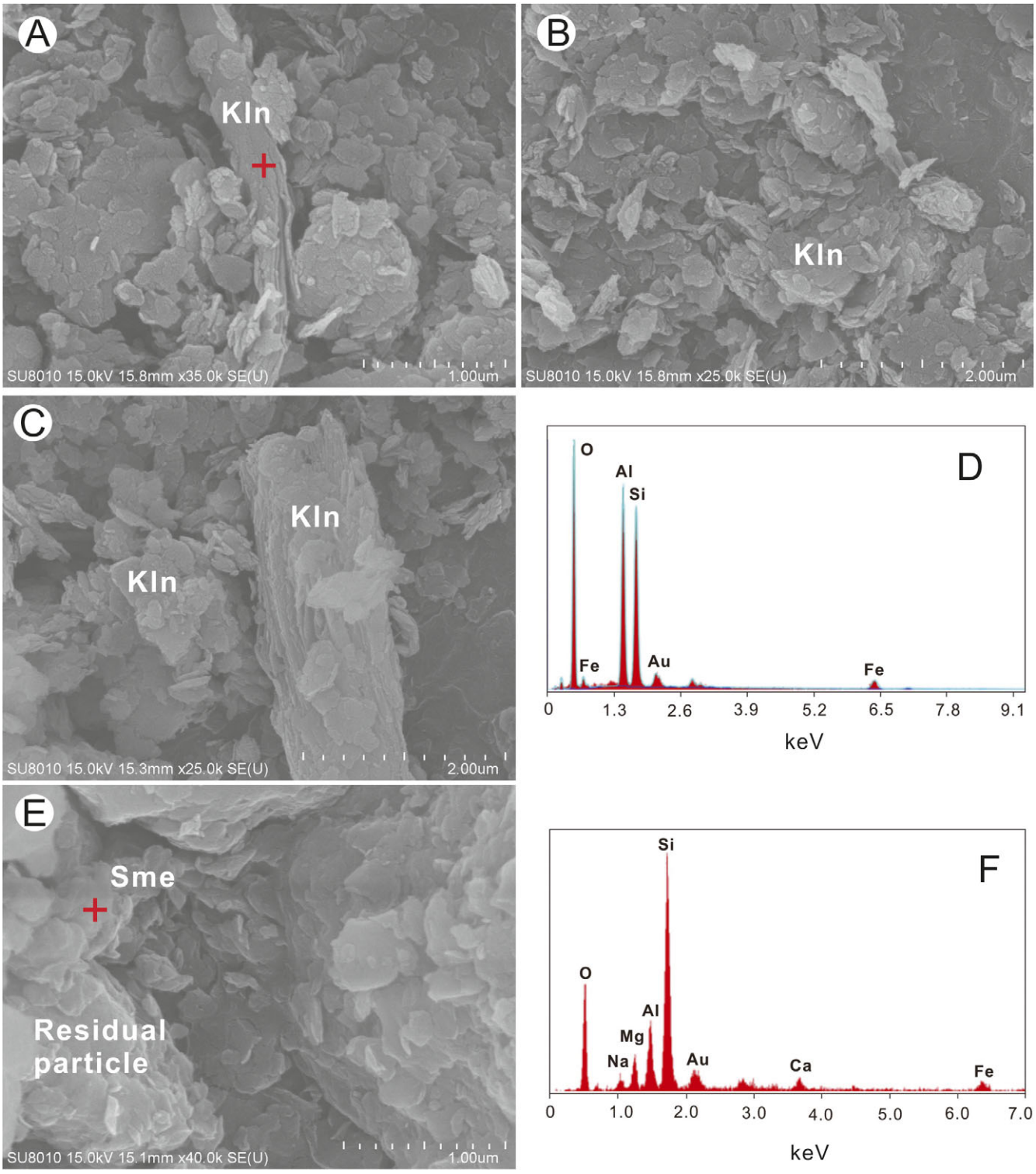

Figure 4. Scanning electron microscopy images of the Nanyang samples. (A) Kaolinite showing a booklet aggregate (E horizon); (B) clay flakes having smooth and flat basal planes with ragged edges (E horizon); (C) clay flakes showing small grain size and poorly developed edge dimension (B horizon); (D) EDS of the particle in A, showing a Si/Al ratio of 0.96, consistent with kaolinite; (E) basalt exhibiting a porous structure with abundant small clay flakes (bedrock); (F) EDS of the clay flakes in E, showing a Si/Al value of 3.83, consistent with smectite. Kln = kaolinite; Sme = smectite.

shows the inverse trend of those of TiO_2 and Fe_2O_3, with modest concentrations in the lower E horizon (28.0–28.5%) relative to other soil horizons (26.0–28.0%). MnO and MgO show generally upward decreasing trends, changing from 0.13 to 0.36% and from 0.31 to 0.80%, respectively. CaO, Na_2O, and K_2O are notably low in the soil profile, with ranges of 0.03–0.05%, 0.000–0.025%, and 0.011–0.020%, respectively. The upper E horizon contains less P_2O_5 (0.10–0.12%) than the lower E, AE and B horizons (0.13–0.23%).

https://doi.org/10.1017/cmn.2024.14 Published online by Cambridge University Press

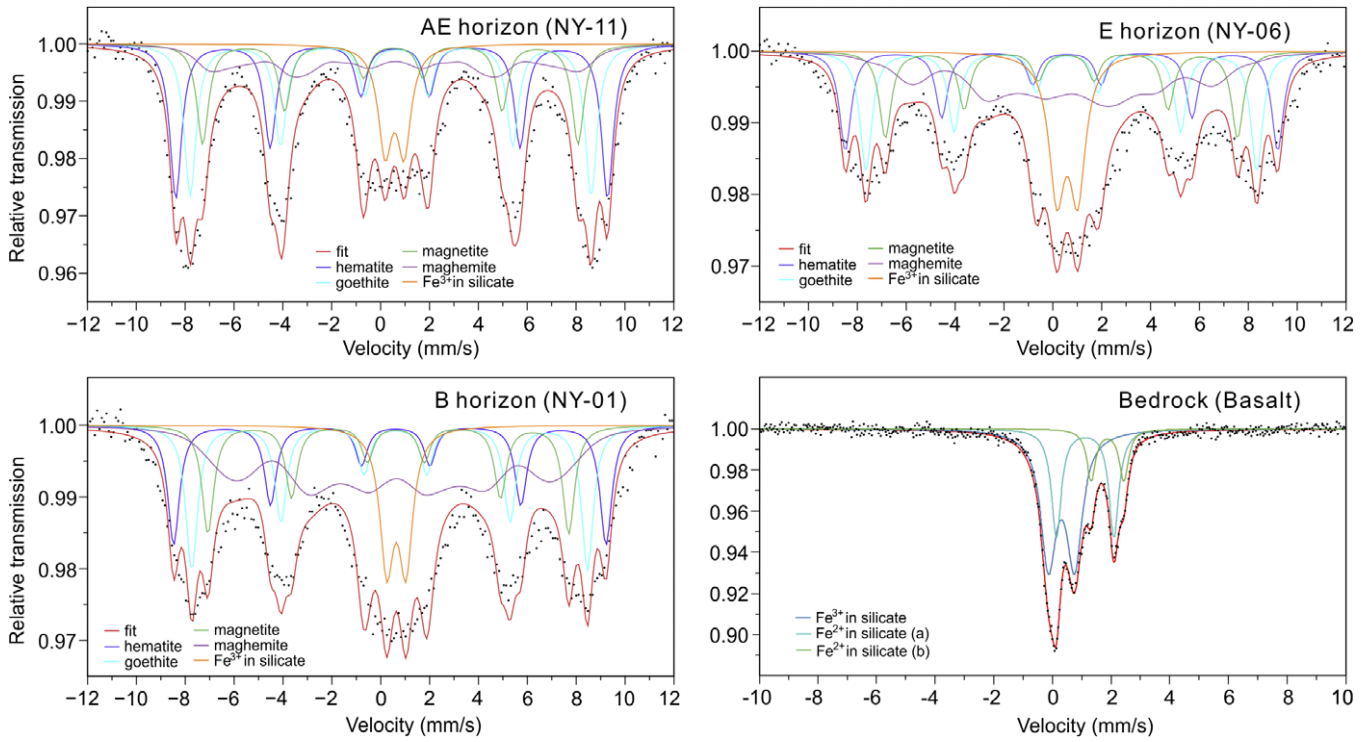

Figure 5. Mössbauer spectra of representative samples showing the presence of maghemite, hematite, magnetite, and goethite in the soil samples, and magnetite and both Fe^{3+} and Fe^{2+} in silicates of the basalt bedrock.

The gain or loss values of the Nanyang soil samples vary greatly along the weathering profile (Fig. 7). Fe, Ti, and Al show slight losses in the upper and lower parts of the profile, but no net change (i.e. reflecting immobility) or even slight accumulations in the middle part of the profile. Mg, Ca, Na, and K show almost complete loss in the weathering products. Si and P leached out intensively, and remain in relatively small amounts, and Mn leached strongly from the upper profile, but exhibited reduced mobility and even weak accumulation in the lower profile.

The $^{56}Fe/^{54}Fe$ values of all soil samples from the weathering regolith are positive, with slightly greater values for samples of the upper profile (+0.12 to +0.19‰) compared with those of the lower profile (+0.06 to +0.09‰), with the sample from the upper E horizon yielding the greatest $^{56}Fe/^{54}Fe$ value (+0.19±0.06‰; Table 3; Fig. 6). The $^{56}Fe/^{54}Fe$ value of the basalt bedrock sample is +0.07±0.02‰, comparable to the average of igneous rocks (Beard et al., 2003). Replicate analyses of the basalt standard BHVO-2 yielded a $\delta^{56}Fe$ value of +0.111±0.031‰, which is identical to the recorded value of +0.128±0.019‰ for this standard within measurement error (Millet et al., 2012).

Discussion

Clay minerals in the Nanyang weathering profile

The Nanyang tholeiitic basalt bedrock is dark gray in color and exhibits an amygdaloidal structure, consisting mainly of smectite and plagioclase with a minor amount of pyroxene. The weathering regolith above the bedrock is generally reddish and markedly loose in structure, consisting uniformly of kaolinite, maghemite, hematite, goethite, magnetite, and a trace amount of quartz, while trace gibbsite is present only in the AE horizon (Figs 3 and 4). The weathering profile exhibits a sharp transition from loose soil material to solid basalt bedrock (Fig. 2e), indicating that mass fluxes driving chemical weathering dominated along textural contrast and weathering-related boundaries (Phillips et al., 2019). The sharpness of this transition reflects the rapid development of regolith on mafic and ultramafic rocks due to the rapid conversion of bedrock to weathered rock compared with acidic igneous and sedimentary rocks, with intense chemical weathering eliminating any trace of the primary mineralogical and geochemical composition of the parent rocks (Phillips et al., 2019; Vilela et al., 2019). The well-developed amygdaloidal texture and columnar joint structure of the parent basalt favored infiltration of groundwater and formation of smectite during basalt weathering (Fig. 2E). In supergene environments, the Si and Al released by dissolution of volcanic materials can lead to oversaturation of sediment porewater with respect to smectite, which is typically the clay mineral phase in thermodynamic equilibrium with pore solutions during basalt weathering (Christidis, 1998; Ziegler et al., 2003).

Smectite typically displays a mixed dioctahedral and trioctahedral structure in relatively weakly weathered basalt bedrock, in which the dioctahedral component is considered to be derived from pedogenic breakdown of inherited trioctahedral smectite due to replacement of Ca, Mg by Al and oxidation of Fe^{2+} to Fe^{3+} (Lessovaia et al., 2016; Hong et al., 2023). Microscopic observations show that cavities and cracks developed intensively in the Nanyang basalt bedrock due to replacement of the original basaltic glass by clay flakes and mechanical disintegration of parent rocks (Fig. 4E). Distinct clay flakes with curled edges and Si/Al ratio of 3.83, the 15 Å reflection in the XRD profile and, in particular, the 1.50 Å and 1.54 Å peaks of smectite (060) reflection indicate the mixed dioctahedral and trioctahedral structure of this smectite (Figs 3 and 4E,F). However, primary hydrothermal alteration during cooling of lava as well as

https://doi.org/10.1017/cmn.2024.14 Published online by Cambridge University Press

Table 1. Fitting parameters and iron phases of the Mössbauer spectra of the Nanyang soil

Sample	Spectra	δ δ (mm s^{-1})	Δ (mm s^{-1})	Γ (mm s^{-1})	H (T)	RA (%)	Iron phase	(Gth+Hem)/(Mag+Mgh)
NY-11	D1	0.572	0.777	0.682		10.2	Fe^{3+} in silicates	
	S1	0.523	–0.143	0.582	54.92	26.5	Hematite	
	S2	0.535	–0.243	0.582	51.00	26.1	Goethite	1.41
	S3	0.462	–0.123	0.582	47.74	17.2	Magnetite	
	S4	0.600	0.00	1.194	38.41	20.0	Maghemite	
NY-10	D1	0.567	0.804	0.682		13.2	Fe^{3+} in silicates	
	S1	0.512	–0.237	0.582	54.62	22.4	Hematite	
	S2	0.450	–0.085	0.582	50.88	20.5	Goethite	0.98
	S3	0.577	–0.365	0.582	47.56	19.9	Magnetite	
	S4	0.497	–0.286	1.094	32.51	24.0	Maghemite	
NY-08	D1	0.594	0.744	0.682		10.9	Fe^{3+} in silicates	
	S1	0.504	–0.225	0.582	55.50	22.9	Hematite	
	S2	0.500	–0.201	0.582	51.00	21.9	Goethite	1.01
	S3	0.511	–0.224	0.582	47.14	17.3	Magnetite	
	S4	0.600	–0.388	1.394	32.99	27.0	Maghemite	
NY-06	D1	0.590	0.850	0.782		16.1	Fe^{3+} in silicates	
	S1	0.466	–0.222	0.582	55.00	17.5	Hematite	
	S2	0.471	–0.247	0.582	49.71	21.1	Goethite	0.85
	S3	0.449	–0.194	0.582	44.80	15.3	Magnetite	
	S4	0.585	–0.388	1.394	28.52	30.0	Maghemite	
NY-03	D1	0.643	0.763	0.682		12.9	Fe^{3+} in silicates	
	S1	0.552	–0.263	0.582	54.29	16.5	Hematite	
	S2	0.548	–0.261	0.582	50.03	20.5	Goethite	0.74
	S3	0.500	–0.240	0.582	45.94	15.1	Magnetite	
	S4	0.650	–0.366	1.394	32.20	35.0	Maghemite	
NY-01	D1	0.637	0.781	0.682		11.1	Fe^{3+} in silicates	
	S1	0.492	–0.240	0.582	55.00	16.6	Hematite	
	S2	0.483	–0.238	0.582	50.34	20.2	Goethite	0.71
	S3	0.467	–0.311	0.582	45.89	15.1	Magnetite	
	S4	0.589	–0.129	1.394	32.64	37.0	Maghemite	
Basalt	D1	0.310	0.886	0.649		57.4	Fe^{3+} in silicates	
	D2	1.12	1.963	0.406		29.7	Fe^{2+} in silicates (a)	
	D3	1.88	1.105	0.373		12.9	Fe^{2+} in silicates (b)	

Notes: δ = isomer shift; Δ = quadrupole shift; Γ = line width; H = magnetic hyperfine field; RA = relative area.

permeating groundwater during supergene weathering often produce trioctahedral smectite in basaltic bedrock (Egli et al., 2008). The surfaces of lava flows are generally vesicular and very porous, and the interior of the rock bodies is usually broken due to well-developed joints. Glassy components in lava flows usually weather faster than crystalline phases such as plagioclase and pyroxene (Marques et al., 2014). Therefore, the dioctahedral smectite in the Nanyang basalt bedrock probably resulted from the gradual transformation of inherited trioctahedral smectite under acidic conditions, as lava flows are highly permeable and susceptible to decomposition and favor the transformation from trioctahedral smectite to dioctahedral smectite during pedogenesis (Lessovaia et al., 2016).

Pedogenesis of the Nanyang basalt protolith under tropical climate conditions has caused complete decomposition of the parent mineral components. The main weathering products are kaolinite and Fe (oxyhydr)oxide minerals phases, while smectite, plagioclase, and pyroxene are lacking. Uniform CIA values of 99.53–99.73 in the weathering regolith (Table 2; Fig. 2) indicate a highly weathering soil with stable secondary mineral phases

https://doi.org/10.1017/cmn.2024.14 Published online by Cambridge University Press

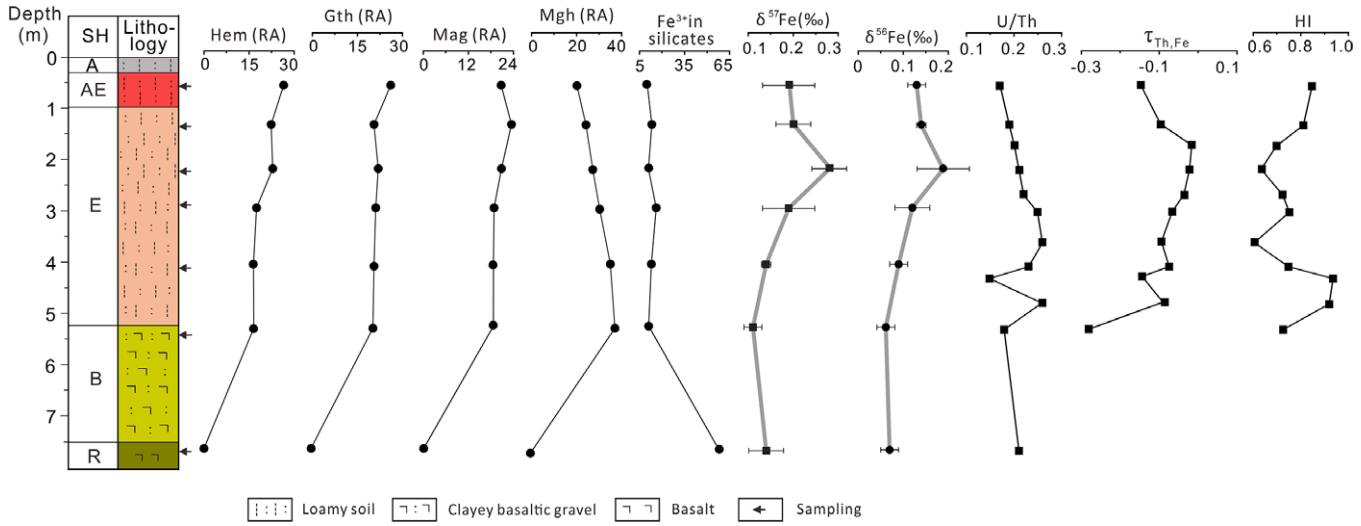

Figure 6. Variation in Fe mineral phases, Fe isotopic values, U/Th ratio, $\tau_{Th,Fe}$, and 'crystallinity' of kaolinite (Hinckley index) in the Nanyang soil profile. SH = soil horizon; A = topsoil; AE = weathering material with trace organic matter in transition between topsoil and leaching layer; E = eluvial horizon consisting of light colored loam; B = accumulation of clays and weathered gravels of decomposing bedrock; R = Rock; HI = Hinckley index; RA = relative area.

(Pokrovsky et al., 2005; Phillips et al., 2019). A similar weathering pattern has been widely reported elsewhere for basalt-derived soils (Rasmussen et al., 2010; Fernández-Caliani and Cantano, 2010; Campodonico et al., 2019). For example, in low-elevation sites of the southern Cascade Range of California, USA, under relatively high mean annual precipitation and temperature conditions, the weathering regolith was characterized by well-developed Alfisols and Ultisols with dominance of secondary kaolins and Fe (oxyhydr) oxides (Rasmussen et al., 2010); in a soils derived from tholeiitic basalt bedrock in subtropical Misiones, NE Argentina, intense weathering led to removal of ~50% of the original basalt mass via solution, and soil in the upper profile consists dominantly of kaolinite and hematite with minor amorphous Fe(Al) (oxyhydr) oxides (Campodonico et al., 2019).

The Hinckley index (HI) of kaolinite in the Nanyang weathering profile ranges from 0.62 to 0.93, indicating in general a relatively disordered crystal structure, consistent with its poorly developed anhedral morphology, as observed under SEM (Fig. 4). However, samples from the middle E horizon exhibit generally less 'crystallinity' compared with those from the lower and upper E horizon and the AE horizon. Changes in 'crystallinity' of kaolinite with position in the soil profile can probably be attributed to the variable leaching intensity of the weathered material.

In advanced weathering profiles, soil minerals are dominated by poorly ordered kaolinite and Fe (oxyhydr)oxides (Qafoku et al., 2004). Kaolinite, which forms through intense chemical weathering, is the dominant clay species in the Nanyang profile, consistent with its notably high CIA values (99.53–99.73). The 'crystallinity' of kaolinite is dependent on the pedogenic and geochemical environment of its formation, transport, and deposition (Pineau et al., 2022). The low 'crystallinity' of kaolinite in subtropical to tropical soils with low organic content is often associated with intense ferrolysis subject to long cycles of anaerobiosis and aerobiosis due to fluctuations between wet and dry climate conditions. Variations in acidity are coupled with ferrolysis and can increase the concentrations of Si and Al in the soil solution, thus favoring the formation of kaolinite crystals of small size and low 'crystallinity' (da Silva et al., 2019).

Fe (oxyhydr)oxide minerals formed in the weathering profile

The Nanyang residual soil formed through intensive removal of Ca, Mg, K, Na, and Si, a process that operates vigorously under oxidizing and acidic conditions (Giorgis et al., 2014; Jiang et al., 2018). In addition to depletion of base cations and silica, weathering of basaltic rocks under tropical climate conditions can mobilize Al and Fe (Perez-Fodich and Derry, 2019). Gibbsite is present only in trace amounts with slightly greater abundance in the upper soil horizons, as shown by its characteristic XRD reflection (Fig. 3). The various soil horizons of the weathering profile have nearly uniform geochemical and mineralogical compositions, with Al_2O_3 content being consistently high (26.0–28.5%) and most Al being resident in kaolinite, suggesting that the relative enrichment of Al was a consequence of chemical leaching of base cations and silica (Lyu et al., 2022).

Ti and Al are considered to be the two most immobile elements during chemical weathering of basalts (Gíslason et al., 1996; Pokrovsky et al., 2005). The Nanyang soil profile exhibits relatively uniform TiO_2/Al_2O_3 values of 0.11–0.14, similar to that of 0.13 for the basalt bedrock, confirming an *in situ* weathering origin of the soil (Table 2). The dissolved Al^{3+} from the octahedral sheet of smectite can precipitate as Al-Fe (oxyhydr)oxides such as gibbsite during flooding of the soil in conjunction with increasing pH (Van Breemen and Buurman, 2002). Gibbsite is commonly observed to form from basalts during intensive chemical leaching under warm and humid climatic conditions. The organic acids released from decomposition of organic matter favor the removal of Al from clay minerals and, thus, enhance dissolution of clay phases (April et al., 2004; Kovács and Czigány, 2017), and the lower pH associated with continuously high moisture conditions promotes the formation of organo-Al complexes and decreases the activity of Al^{3+} and Al-hydroxocomplexes in the soil solution (Drever and Stillings, 1997; Lyu et al., 2022; Watanabe et al., 2023). The limited variation of Al and precipitation of only trace amounts

https://doi.org/10.1017/cmn.2024.14 Published online by Cambridge University Press

Table 2. Major element chemistry and CIA index of alteration of soil samples from the Nanyang basalt weathering profile

Soil horizon	Sample	SiO_2 (wt.%)	TiO_2 (wt.%)	Al_2O_3 (wt.%)	Fe_2O_3 (wt.%)	MnO (wt.%)	MgO (wt.%)	CaO (wt.%)	Na_2O (wt.%)	K_2O (wt.%)	P_2O_5 (wt.%)	LOI (wt.%)	SUM (wt.%)	Th (10^{-6})	U (10^{-6})	U/Th	TOC (wt.%)	CIA	TiO_2/Al_2O_3	Fe_2O_3/Al_2O_3
AE	NY-11	33.46	3.57	27.98	21.97	0.13	0.33	0.05	0.018	0.020	0.135	12.32	99.98	5.69	1.00	0.17	0.27	99.53	0.13	0.79
E	NY-10	33.61	3.68	27.47	22.19	0.14	0.44	0.04	0.022	0.016	0.115	11.92	99.65	5.43	1.04	0.19	0.17	99.56	0.13	0.81
	NY-09	34.15	3.47	27.96	20.91	0.16	0.45	0.04	0.008	0.014	0.102	12.14	99.40	4.69	0.95	0.20	0.17	99.62	0.12	0.75
	NY-08	33.93	3.86	27.75	21.54	0.24	0.34	0.04	0.009	0.016	0.116	11.79	99.63	4.87	1.03	0.21	0.16	99.62	0.14	0.78
	NY-07	34.48	3.88	28.04	21.41	0.13	0.31	0.04	0.018	0.016	0.118	11.78	100.22	4.92	1.07	0.22	0.13	99.57	0.14	0.76
	NY-06	33.62	3.67	27.57	21.92	0.15	0.44	0.03	0.003	0.013	0.169	12.17	99.75	5.19	1.27	0.25	0.12	99.71	0.13	0.79
	NY-05	35.88	3.21	28.05	19.20	0.21	0.65	0.04	0.025	0.012	0.134	12.25	99.67	4.69	1.20	0.26	0.10	99.58	0.11	0.68
	NY-04	35.08	3.39	28.47	19.85	0.16	0.80	0.04	0.014	0.011	0.130	12.34	100.27	4.74	1.08	0.23	0.10	99.65	0.12	0.70
	NY-03	34.41	3.70	27.59	21.88	0.24	0.46	0.04	0.002	0.012	0.141	11.99	100.46	5.65	0.85	0.15	0.10	99.70	0.13	0.79
	NY-02	33.79	3.40	27.90	21.54	0.36	0.61	0.03	0.000	0.013	0.226	12.53	100.38	5.23	1.08	0.21	0.11	99.73	0.12	0.77
B	NY-01	37.20	3.66	26.05	20.52	0.29	0.50	0.04	0.018	0.018	0.180	11.18	99.64	6.29	1.11	0.18	0.13	99.57	0.14	0.79
Bedrock	Basalt	50.20	1.77	13.90	10.90	0.12	7.22	8.81	2.62	0.29	0.26	1.53	97.62	2.41	0.51	0.21	/	/	0.13	0.78

Notes: Total Fe is the sum of FeO and Fe_2O_3; LOI is loss on ignition; CIA = $(Al_2O_3/(Al_2O_3 + CaO^* + K_2O + Na_2O) \times 100\%$ (Nesbitt and Young, 1982); Th and U values from inductively coupled plasma mass spectrometry (ICP-MS) analysis in unpublished observations.

of gibbsite in the weathering profile, as documented by mass transport calculations (Fig. 7), indicate that chemical weathering of the Nanyang soil did not experience extreme weathering leading to Al mobility, probably due to insufficient time or lack of highly acidic (pH<4.5) conditions (Giorgis et al., 2014). Fe_2O_3/Al_2O_3 values range from 0.68 to 0.81 with only slight fluctuations through the soil profile and little deviation from the 0.78 ratio of the basaltic bedrock (Table 2), suggesting that pedogenesis at Nanyang did not cause Fe (or Al) enrichment. An increase in Fe^{3+} activity can result in increasing substitution of Fe for Al in the kaolinite structure and, as a result, reducing its 'crystallinity' as it becomes increasingly disordered (Yang et al., 2001). At Nanyang, intensive oxidation and lixiviation occurred in the upper soil profile, resulting in downward penetration of weakly acid to weakly alkaline soil waters (He et al., 2008; Jiang et al., 2018). The underlying soil, especially the middle E horizon (Fig. 6), experienced intense eluviation as a result of the increasing solubility of Si and Al and, in particular, the increasing activity of Fe^{3+}. These processes not only impeded the growth of kaolinite crystals, but also facilitated the isomorphic substitution of Al by Fe in the kaolinite structure, thereby generating a more poorly crystalline form of kaolinite in the middle E horizon (Yang et al., 2001; Lima et al., 2021).

Iron in the Nanyang basaltic protolith is present as both Fe^{3+} and Fe^{2+} in silicates and pyroxenes and magnetite, but exclusively as Fe^{3+} in Fe (oxyhydr)oxides (maghemite, hematite, magnetite, and goethite) and phyllosilicate of the weathering profile (Table 1; Fig. 5). In the B horizon, a significant increase of Fe_2O_3 content (20.5%) compared with the bedrock (10.9%) indicates that Fe accumulated during the leaching of alkalis, Si, Ca, and Mg. Field evidence of Fe mobility and reprecipitation in the Nanyang soil profile includes the greyish white color of the soil matrix of the E and B horizons, a well-developed mottle structure in the E horizon, and filling of Fe- and Mn- (oxyhydr)oxide nodules and concretions in fissure and macropore networks of the soil matrix in the E and B horizons (Fig. 2C,D). These features suggest that iron migration and reprecipitation occur at the initial stage of basalt weathering, as iron can be transported in the ferrous state either in the form of Fe^{2+} or $Fe(OH)^{3-}$ during initial weathering of igneous rocks (Christidis, 1998), resulting in the light-color soil matrix and an enrichment of Fe (oxyhydr)oxides in the millimeter- to centimeter-scale cracks and fissures in the saprolite (Kovács and Czigány, 2017; Yu et al., 2020; Santos et al., 2021). As chemical weathering proceeded, the selective leaching of associated bases gradually increased upwards, and finally resulted in strong Si depletion and Fe and Al enrichment in the soil profile. Fe (oxyhydr)oxides are the main residual minerals of basalt weathering, with the exact composition of the secondary Fe phases being determined by parent lithology and climate (rainfall and temperature), especially the redox and drainage conditions of the soil profile (Driese, 2004; Marques et al., 2014).

Mineralogical compositions as well as the geochemical indexes of the Nanyang weathering regolith suggest that lateritization developed as a continuous process. The formation of secondary Fe (oxyhydr)oxide minerals (especially hematite and goethite) is believed to be controlled mainly by climatic and drainage conditions, while maghemite in regolith from weathering of mafic rocks is primarily a product of oxidation of magnetite in the bedrock (da Costa et al., 1999). The abundant maghemite in the Nanyang soil was generated primarily by weathering under warm and humid climate conditions (Lu et al., 2008; Ayoubi and

https://doi.org/10.1017/cmn.2024.14 Published online by Cambridge University Press

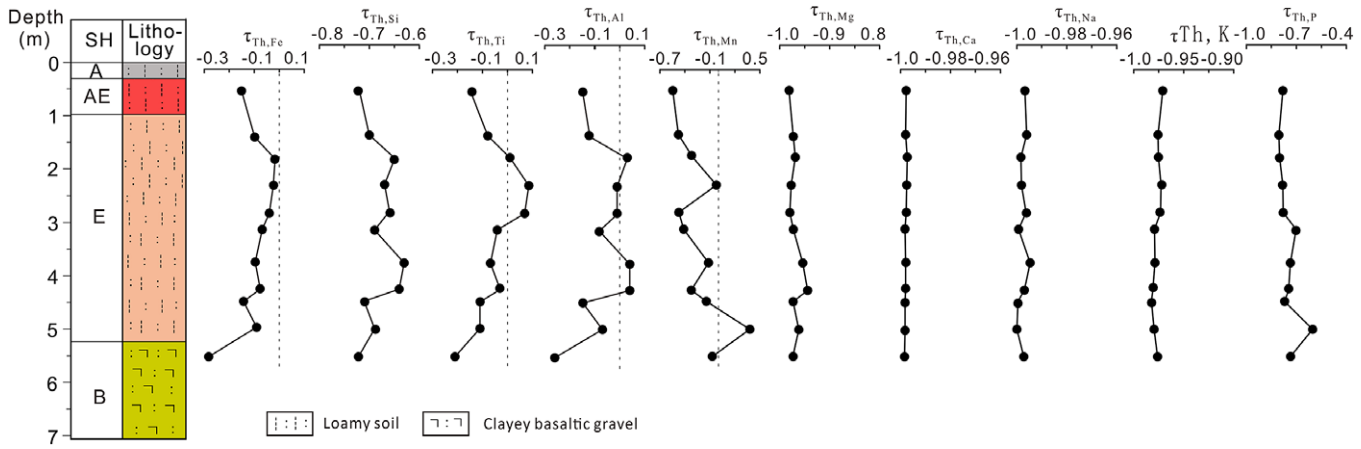

Figure 7. Gain/loss profiles of major elements in the Nanyang soil profile. For definitions, see Fig. 6.

Table 3. Iron isotopic values of selected Nanyang soil samples (‰)

Soil horizon	Sample	$^{56}Fe/^{54}Fe$	2SD	$^{57}Fe/^{54}Fe$	2SD	$^{57}Fe/^{56}Fe$	2SD
AE (20–100 cm)	NY–11	0.13	0.02	0.19	0.06	0.07	0.05
E (100–520 cm)	NY–10	0.14	0.01	0.20	0.04	0.07	0.05
	NY–08	0.19	0.06	0.28	0.04	0.09	0.03
	NY–06	0.12	0.04	0.19	0.06	0.07	0.03
	NY–03	0.09	0.02	0.14	0.01	0.06	0.00
B (520–770 cm)	NY–01	0.06	0.02	0.11	0.02	0.04	0.03
Bedrock	Basalt	0.07	0.02	0.14	0.04	0.06	0.01
Standard	BHVO–2	0.11	0.03	0.14	0.06	0.03	0.02

Adman, 2019). Upward in the soil profile, from the B horizon to the AE horizon, the RA value of maghemite decreases markedly from 37.0% to 20.0%, whereas those of hematite and goethite increase gradually from 16.6% to 26.6% and from 20.2% to 26.1%, respectively, while that of magnetite shows only a minor change from 15.1% to 17.2% (Table 1; Fig. 6). Although magnetite occurs widely as an accessory mineral in basaltic rocks, magnetite was not detected in the Nanyang basalt bedrock in the Mössbauer measurement, suggesting that lithogenic magnetite in the Nanyang soil is negligible. This pattern suggests that evolution of Fe (oxyhydr)oxides with weathering was dominated by transformation from maghemite to hematite, goethite, and magnetite. Unlike the lateritic soils on fluvial deposits in south China, in which ferrihydrite occurs widely as the precursor mineral of other thermodynamically stable Fe (oxyhydr)oxide minerals (Hong et al., 2016), ferrihydrite was not observed in the Nanyang soil (Qi et al., 2022), suggesting that the small organic-matter content in soil favored the mineral evolution toward greater oxidation and more crystalline levels (Pizarro et al., 2017) and the formation of Fe (oxyhydr)oxide minerals in Nanyang soil involved limited biogenic iron as ferrihydrite often precipitates via biotic pathways (Melton et al., 2014; Yu et al., 2019; Klaes et al., 2023). Maghemite is a metastable Fe (oxyhydr)oxide phase that transforms to other stable phases during weathering. An oxic and arid environment causes the transformation of magnetite to hematite and, inversely, reduced oxygen fugacity causes the transformation of hematite to magnetite (Giorgis et al., 2014; Long et al., 2015). The formation of magnetite involves reduction of Fe^{3+} to Fe^{2+} and occurs usually in well-drained, oxidizing soils, which is often linked to soil humidity fluctuations. Conversely, oxidation of Fe^{2+} to Fe^{3+} favors the formation of maghemite, which can further transform into hematite, a process that is facilitated by a warm and dry environment (Ahmed and Maher, 2018).

Upward within the Nanyang soil profile, the (Gth+Hem)/(Mag +Mgh) ratio increases from 0.71 to 1.41 (Table 1), suggesting that, in a humid weathering environment, pedogenetic transformations of Fe (oxyhydr)oxide minerals are dominated by conversion of strongly magnetic magnetite and maghemite into hematite and goethite (Lu et al., 2008; Liu et al., 2022). Basaltic weathering profiles are often observed consisting mainly of poorly crystalline minerals such as ferrihydrite, allophane, imogolite, and opaline silica, which are unstable soil components that evolve with time into crystalline phases (Chadwick et al., 2003). In subtropical Paraná (Brazil) with a seasonally hot and cold climate, Fe (oxyhydr)oxides in the basalt-derived Ferralsol are mainly hematite, maghemite, and magnetite (Cervi et al., 2014). At an advanced to extreme weathering stage, such profiles consist dominantly of pedogenic phyllosilicates and Fe- and Al-Fe (oxyhydr)oxides and sesquioxides (goethite, hematite, and gibbsite) (Liivamägi et al., 2018). The Nanyang basaltic weathering profile is dominated by kaolinite and stable Fe (oxyhydr)oxides, with trace gibbsite, which is especially characteristic of weathering profiles developed on basalt under humid and/or warm climates, in which bases and silica have been almost completely lost through leaching.

In large geographic regions under temperate to semi-arid climate conditions, soil magnetic susceptibility exhibits positive correlation with mean annual temperature and precipitation due to the formation of pedogenic magnetite and maghemite (Grimley and Vepraskas, 2000; Geiss et al., 2004). However, in temperate and tropical regions Fe (oxyhydr)oxides in soils occur dominantly in the form of crystalline Fe phases, and goethite and hematite are the most abundant Fe (oxyhydr)oxide minerals due to transformation from ferrimagnets (Hu et al., 2009; Liu et al., 2012). The formation of goethite depends largely on environmental moisture, and oxic and acidic conditions favor the maghemite-to-goethite transformation (da Silva et al., 2019). In more poorly drained soils, other Fe (oxyhydr)oxides such as maghemite and magnetite may exist independent of the climate

https://doi.org/10.1017/cmn.2024.14 Published online by Cambridge University Press

conditions (Claudio et al., 2017). Highly weathering soils (Oxisols, Ultisols, and Alfisols) from mafic igneous rocks in subtropical to tropical southern Brazil contain mainly hematite and maghemite in soils at different landscape positions, and maghemite is primarily formed by weathering of bedrock (da Costa et al., 1999). In the adjacent basalt-derived regolith on the same bedrock with the Nanyang soil, only hematite and goethite were observed as Fe (oxyhydr)oxide minerals throughout the soil profile (Qi et al., 2022). However, in the Nanyang soil, maghemite, hematite, goethite, and magnetite co-exist throughout the soil profile. This assemblage of Fe (oxyhydr) oxide minerals in soil suggests that the tropical monsoonal climate and poorly drained soil conditions have produced a seasonally wet/dry environment that promoted formation of the paragenetic Fe (oxyhydr)oxide phases of magnetite, maghemite, hematite, and goethite, as tropical monsoonal conditions favor the neoformation of fine-grained magnetite and the mineral transformations due to maghemitization and hematization (Ouyang et al., 2015). Thus, except for the influence of the parent material lithology, pedogenic Fe (oxyhydr)oxide minerals in highly weathered soils under subtropical to tropical climates are also dominantly influenced by soil moisture (drained condition), redox, and acidic conditions, which cause perturbations in use of iron mineral-based paleoclimatic proxies such as soil magnetic property and hematite-goethite value.

Weathering processes indicated by secondary minerals of the Nanyang soil

The Nanyang soil profile has a quite uniform Fe_2O_3 content, varying within a narrow range from 19.2% to 22.2%, with generally smaller values for samples from the middle E horizon (Table 2). Iron isotope compositions ($\delta^{57}Fe$ and $\delta^{56}Fe$) exhibit similar secular trends and vary within narrow ranges through the soil profile. $\delta^{57}Fe$ ranges from +0.11‰ in the B horizon to +0.28‰ in the middle E horizon, and $\delta^{56}Fe$ ranges from +0.06‰ to +0.19‰, respectively. The highest values for $\delta^{57}Fe$ (+0.28‰) and $\delta^{56}Fe$ (+0.19‰) were observed in the same sample (NY-08) from the middle E horizon, whereas the lowest values $\delta^{57}Fe$ (+0.11‰) and $\delta^{56}Fe$ (+0.06‰) were found in sample NY-01 from the B horizon. Although the B horizon displays differences in its mineralogical and geochemical composition from the bedrock (Table 2; Fig. 3), their iron isotopic compositions are identical, suggesting that iron phases formed at an early stage of weathering retain the isotopic composition of the parent rock. Other samples from the AE and E horizons show slightly heavy $\delta^{57}Fe$ and $\delta^{56}Fe$ signatures that are significantly above the parent rock values, reflecting the progressive removal of isotopically lighter Fe during intense chemical weathering.

The various horizons of the Nanyang soil profile show uniform Fe mineralogy. The amounts of hematite, goethite, and magnetite generally increase upward from the B horizon to the AE horizon, whereas the amount of maghemite exhibits the opposite trend. The Fe_2O_3 contents of the soil horizons fluctuate within a limited range, from 19.20% to 22.19%. The isotopically heavy iron samples do not show a distinct relationship with Fe_2O_3 content (Table 2; Fig. 6). However, the highest $\delta^{57}Fe$ and $\delta^{56}Fe$ values are observed in the leached E horizon, and samples from the AE and E horizons have relatively heavier Fe isotopic signatures, suggesting that weathering processes in the Nanyang soil profile generate solid-phase materials that are ^{57}Fe- and ^{56}Fe-enriched relative to the unweathered basalt rock. Samples with heavier isotopic signatures are characterized by less Fe mobilization (Figs 6 and 7), although iron loss relative to the parent rock occurred in nearly all soil horizons. The strong positive correlation (R^2=0.77, n=6, ρ<0.05) between the gain or loss of Fe and $\delta^{56}Fe$ indicates that preferential removal of isotopically lighter Fe occurred during pedogenesis (Fig. 8).

Th and U are both relatively immobile during weathering, but strongly oxidizing conditions – in which U^{4+} is insoluble and U^{6+} is soluble – favor the solubility of U and decrease the U/Th ratio (Sheldon and Tabor, 2009). The basaltic bedrock has a U/Th ratio of 0.21 (Table 2; Fig. 6). The lower U/Th ratios of the upper soil horizons (0.17–0.19) suggest that U was leached away while Th was retained due to the intensely oxidizing conditions, and that the elevated U/Th ratios in the mid-lower B horizon (0.23–0.26) indicate a re-distribution and lessivage process as well as a redox gradient in the lower part of the soil profile. Variations of U/Th in the lower soil profile probably reflect redox fluctuations in concert with changes in groundwater conditions, as also indicated by variability in the 'crystallinity' of kaolinite through the soil

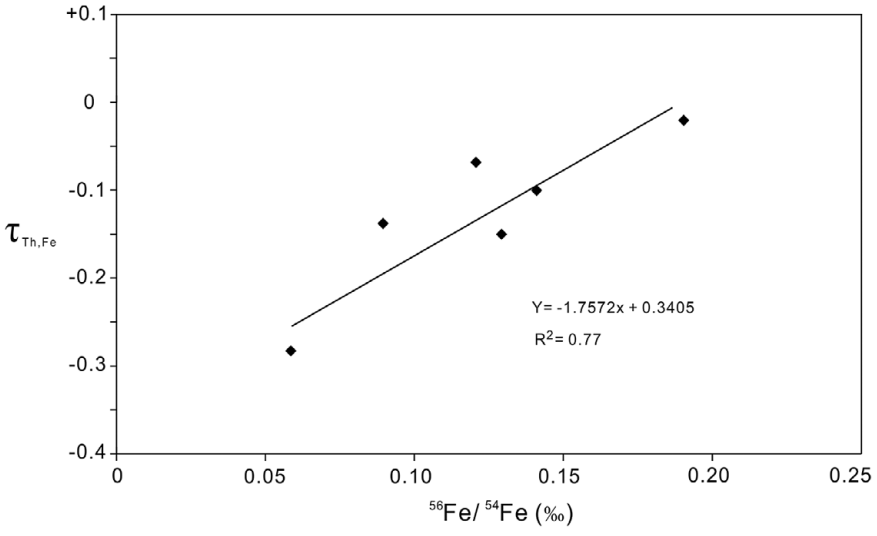

Figure 8. Correlation between Fe isotopic composition ($^{56}Fe/^{54}Fe$) and mass transfer coefficient of Fe ($\tau_{Th,Fe}$).

https://doi.org/10.1017/cmn.2024.14 Published online by Cambridge University Press

profile. The uniformly high CIA values (99.53–99.73) of all horizons of the Nanyang soil profile reflect the overall intensity of chemical weathering, with strongly oxidizing conditions indicated by smaller U/Th ratios in the upper horizons, in association with stronger Fe mobilization (i.e. smaller $\tau_{Th,Fe}$ values), which supports a more prolonged and thorough weathering of the upper soil horizons.

In the Nanyang soil, $\delta^{56}Fe$ is negatively correlated with the U/Th value, reflecting that the elevated $\delta^{56}Fe$ results from the intensely oxidizing conditions. The retention of isotopically heavier Fe in the upper Nanyang soil profile can be attributed to the presence of organic matter and microbial activity, which served to promote reductive dissolution of ferric (oxyhydr) oxides instead of a pure inorganic chemical process (Vepraskas and Faulkner, 2001; Ma et al., 2007). Soil organic matter consists of a heterogeneous mixture of organic compounds of various origins, generated from plants or microbial molecules or their monomers, and decomposition of organic matter can produce dissolved components ranging from simple amino acids to high-molecular weight complexes (Basile-Doelsch et al., 2020). Dissolved organic matter can be intensively produced from plant litter, soil humus, microbial biomass, and root exudates in the upper soil horizons, producing a solution that is relatively rich in organic matter (Basile-Doelsch et al., 2020). The TOC value of the Nanyang soil changes from 0.27 to 0.10% down the profile, with generally more TOC in the upper soil horizons and correlating positively to $\delta^{57}Fe$ and $\delta^{56}Fe$ signatures (Tables 2 and 3), suggesting that organic matter facilitates the mobilization and re-distribution of Fe during weathering (Ma et al., 2007; Dauphas et al., 2017; Klaes et al., 2023). The reductively dissolved Fe^{2+} and complexed Fe^{3+} released into soil solution are considerably lighter isotopically than their parent material, and the repetitive removal of Fe from the dynamic upper soil horizons will lead to a progressively increasing heavier Fe in the upper soil profile due to preferential release of ^{54}Fe (Schuth et al., 2015; Wu et al., 2019).

In the mid–lower sections of the Nanyang soil, the low chroma (<3) soil matrix colors and the presence of Fe (oxyhydr)oxides as well as Fe (oxyhydr)oxide nodules and concretions in soil macropores indicate the mobility of iron during the weathering process (Fig. 2C,D). Fe (oxyhydr)oxides formed in soils from oxic weathering of granite in the Swiss Alps contained usually more light Fe isotopes, which was attributed to a kinetically controlled isotope fractionation effect in which light Fe preferentially released from the primary phyllosilicates during weathering of iron-bearing phyllosilicates in soils (Kiczka et al., 2011). In soil developed from peridotite weathering in the tropical Southern Philippines, small Fe isotopic fractionation between the peridotite ($\delta^{56}Fe$=−0.03‰) and the extremely weathered saprolite ($\delta^{56}Fe$=+0.10‰) was regarded as a Rayleigh distillation process based on the correlation with Fe content (Li et al., 2017). However, the comparable $\delta^{56}Fe$ (+0.06‰) of the highly weathered B horizon to that (+0.07‰) of the bedrock in the Nanyang soil profile suggests that Fe (oxyhydr) oxides formed from extreme oxidation of iron(II)-bearing minerals in the bedrock without Fe-isotopic fractionation, instead of preferential dissolution of primary iron-bearing phyllosilicates or a Rayleigh distillation process during weathering of iron(II)-bearing minerals (Table 3). The uniform depth distribution of iron content suggests that pedogenic conditions in the Nanyang soil did not induce significant iron translocations within the profile but, rather, in short-distance mobility and reprecipitation within the soil horizon.

Conclusions

The soil developed from the Nanyang tholeiitic basaltic bedrock consists uniformly of kaolinite, Fe (oxyhydr)oxide minerals, and trace amounts of quartz, while trace gibbsite is present only in the AE horizon. Dioctahedral smectite in the basaltic bedrock was probably produced via transformation of inherited trioctahedral smectite under acidic pedogenic conditions, and the low 'crystallinity' of kaolinite in the Nanyang soil is attributed to intense ferrolysis due to fluctuations between wet/dry climate conditions.

The tropical monsoonal climate and the poorly drained conditions at Nanyang favored a seasonally wet/dry environment and resulted in the distinct paragenetic Fe phases of magnetite, maghemite, hematite, and goethite. Maghemite formed primarily as a product of weathering of bedrock, and the evolution of iron phases with weathering was dominated by transformation from maghemite to hematite, goethite, and magnetite. Pedogenic Fe (oxyhydr)oxide minerals in basalt-derived soils are influenced not only by temperature and rainfall, but also by a number of factors such as drainage, redox, and acidic conditions; thus soil magnetic properties and relative contents of Fe (oxyhydr)oxide minerals of highly weathering soils could not be used as paleoclimatic proxies.

Iron loss occurred for nearly all horizons with respect to the parent rock and showed negligible vertical re-distribution, with a uniform Fe_2O_3 content of 19.2–22.2% between the soil horizons. The $\delta^{56}Fe$ ranges from +0.06‰ in the B horizon to +0.19‰ in the middle E horizon, and the extremely weathered saprolite has the same Fe isotopic composition as the bedrock. Heavier isotopic signatures correspond positively to less Fe mobilization but much more intense oxidizing conditions. The elevated heavier Fe isotopic values may be associated with organic matter and microbial activity due to the reductive dissolution of ferric (oxyhydr)oxides.

Author contribution. H.L.H. conceived, designed, and performed the research and wrote the paper. J.W.W., C.W.W., C.L., L.L.Z., L.Z., D.Q.Z., and Q.F. performed some aspects of the research. T.J.A. co-wrote and edited the paper.

Acknowledgements. The authors thank Dr Z.Q. Zhong and X.W. Zhang for assistance in sample collection; they are also grateful to Dr Joseph W. Stucki, the Editor-in-Chief, to the Associate Editor and to two anonymous reviewers for their insightful reviews, valuable comments, and constructive suggestions

Financial support. This work was supported by the National Natural Science Foundation of China (Projects 42172045, 41972040, and 42002042), the Fundamental Research Funds for the Central Universities, and China University of Geosciences (Wuhan) (no. CUG170106).

Competing interest. The authors declare no competing interests.

Data availability statement. All raw data and results including the images are available upon request.

References

Ahmed, I.A.M., & Maher, B.A. (2018). Identification and paleoclimatic significance of magnetite nanoparticles in soils. *Proceedings of the National Academy of Sciences of the USA*, *115*, 1736–1741.

April, R.H., Keller, D., & Driscoll, C.T. (2004). Smectite in Spodosols from the Adirondack Mountains of New York. *Clay Minerals*, *39*, 99–103.

Ayoubi, S., & Adman, V. (2019). Iron mineralogy and magnetic susceptibility of soils developed on various rocks in western Iran. *Clays and Clay Minerals*, *67*, 217–227.

https://doi.org/10.1017/cmn.2024.14 Published online by Cambridge University Press

Basile-Doelsch, I., Balesdent, J., & Pellerin, S. (2020). Reviews and syntheses: the mechanisms underlying carbon storage in soil. *Biogeosciences*, *17*, 5223–5242.

Beard, B.L., Johnson, C.M., Skulan, J.L., Nealson, K.H., Cox, L., & Sun, H. (2003). Application of Fe isotopes to tracing the geochemical and biological cycling of Fe. *Chemical Geology*, *195*, 87–117.

Biddle, D.L., Chittleborough, D.J., & Fitzpatrick, R.W. (1998). An algorithm to model mass balances quantitatively. *Computers & Geosciences*, *24*, 77–82.

Borker, J., Hartmann, J., Romero-Mujalli, G., & Li, G.J. (2019). Aging of basalt volcanic systems and decreasing CO_2 consumption by weathering. *Earth Surface Dynamics*, *7*, 191–197.

Brantley, S. L., Shaughnessy, A., Lebedeva, M. I., & Balashov, V. N. (2023). How temperature-dependent silicate weathering acts as Earth's geological thermostat. *Science*, *379*, 382–389.

Brimhall, G.H., & Dietrich, W.E. (1987). Constitutive mass balance relations between chemical composition, volume, density, porosity, and strain in metasomatic hydrochemical systems: results on weathering and pedogenesis. *Geochimica et Cosmochimica Acta*, *51*, 567–587.

Campodonico, V.A., Pasquini, A.I., Lecomte, K.L., García, M.G., & Depetris, P.J. (2019). Chemical weathering in subtropical basalt-derived laterites: a mass balance interpretation (Misiones, NE Argentina). *Catena*, *173*, 352–366.

Caner, L., Radtke, L.M., Vignol-Lelarge, M.L., Inda, A.V., Bortoluzzi, E.C., & Mexias, A.S. (2014). Basalt and rhyo-dacite weathering and soil clay formation under subtropical climate in southern Brazil. *Geoderma*, *235–236*, 100–112.

Cervi, E.C., da Costa, A.C.S., & de Souza Junior, I.G. (2014). Magnetic susceptibility and the spatial variability of heavy metals in soils developed on basalt. *Journal of Applied Geophysics*, *111*, 377–383.

Chadwick, O.A., Gavenda, R.T., Kelly, E.F., Ziegler, K., Olson, C.G., Elliot, W.C., & Hendricks, D.M. (2003). The impact of climate on the biogeochemical functioning of volcanic soils. *Chemical Geology*, *202*, 195–223.

Christidis, G.E. (1998). Comparative study of the mobility of major and trace elements during alteration of an andesite and a rhyolite to bentonite, in the islands of Milos and Kimolos, Aegean, Greece. *Clays and Clay Minerals*, *46*, 379–399.

Claudio, C., di Iorio, E., Liu, Q.S., Jiang, Z.X., & Barrón, V. (2017). Iron oxide nanoparticles in soils: environmental and agronomic importance. *Journal of Nanoscience and Nanotechnology*, *17*, 4449–4460.

Craddock, P.R., & Dauphas, N. (2011). Iron isotopic compositions of geological reference materials and chondrites. *Geostandards and Geoanalytical Research*, *35*, 101–123.

da Costa, A.C., Bigham, J.M., Rhoton, F.E., & Traina, S.A. (1999). Quantification and characterization of maghemite in soils derived from volcanic rocks in southern Brazil. *Clays and Clay Minerals*, *47*, 466–473.

da Silva, L.F., Fruett, T., Zinn, Y.L., Inda, A.V., & do Nascimento, P.C. (2019). Genesis, morphology and mineralogy of Planosols developed from different parent materials in southern Brazil. *Geoderma*, *341*, 46–58.

Dauphas, N., John, S., & Rouxel, O. (2017). Iron isotope systematics. *Reviews in Mineralogy and Geochemistry*, *82*, 415–510.

de Jong, E., Kozak, L.M., & Rostat, H.P.W. (1999). Effects of parent materials and climate on the magnetic susceptibility of Saskatchewan soils. *Journal Soil Science*, *80*, 135–142.

Dessert, C., Dupre, B., Gaillardet, J., Francois, L.M., & Allegre, C.J. (2003). Basalt weathering laws and the impact of basalt weathering on the global carbon cycle. *Chemical Geology*, *202*, 257–273.

Drever, J.I., & Stillings, L.L. (1997). The role of organic acids in mineral weathering. *Colloids and Surfaces A: Physicochemical and Engineering Aspects 120*, 167–181.

Driese, S.G. (2004). Pedogenic translocation of Fe in modern and ancient Vertisols and implications for interpretations of the Hekpoort Paleosol (2.25 Ga). *Journal of Geology*, *112*, 543–560.

Dupré, B., Dessert, C., Oliva, P., Goddéris, Y., Viers, J., Francois, L., Millot, R., & Gaillardet, J. (2003). Rivers, chemical weathering and Earth's climate. *Comptes Rendus Geoscience*, *335*, 1141–1160.

Egli, M., Nater, M., Mirabella, A., Raimondi, S., Plötze, M., & Alioth, L. (2008). Clay minerals, oxyhydroxide formation, element leaching and humus development in volcanic soils. *Geoderma*, *143*, 101–114.

Fernández-Caliani, J.C., & Cantano, M. (2010). Intensive kaolinization during a lateritic weathering event in South-West Spain: mineralogical and geochemical inferences from a relict paleosol. *Catena*, *80*, 23–33.

Geiss, C.E., Zanner, C.W., Banerjee, S.K., & Minott, J. (2004). Signature of magnetic enhancement in a loessic soil in Nebraska, United States of America. *Earth and Planetary Science Letters*, *228*, 355–367.

Giorgis, I., Bonetto, S., Giustetto, R., Lawane, A., Pantet, A., Rossetti, P., Thomassin, J.H., & Vinai, R. (2014). The lateritic profile of Balkouin, Burkina Faso: geochemistry, mineralogy and genesis. *Journal of African Earth Sciences*, *90*, 31–48.

Gíslason, S.R., Arnórsson, S., & Ármannsson, H. (1996). Chemical weathering of basalt in southwest Iceland: effects of runoff, age of rocks and vegetative/glacial cover. *American Journal of Science*, *296*, 837–907.

Grimley, D.A., & Vepraskas, M.J. (2000). Magnetic susceptibility for use in delineating hydric soils. *Soil Science Society of America Journal*, *64*, 2174–2180.

Grogan, K.L., Gilkes, R.J., & Lottermoser, B.G. (2003). Maghemite formation in burnt plant litter at East Trinity, North Queensland, Australia. *Clays and Clay Minerals*, *51*, 390–396.

Guggenheim, S., Bain, D.C., Bergaya, F., Brigatti, M.F., Drits, V.A., Eberl, D.D., Formoso, M.L.L., Galán, E., Merriman, R.J., Peacor, D.R., Stanjek, H., & Watanabe, T. (2002). Report of the Association Internationale Pour l'étude des Argiles (AIPEA) Nomenclature Committee for 2001: Order, disorder and crystallinity in phyllosilicates and the use of the 'crystallinity index'. *Clays and Clay Minerals*, *50*, 406–409.

He, Y., Li, D.C., Velde, B., Yang, Y.F., Huang, C.M., Gong, Z.T., & Zhang, G.L. (2008). Clay minerals in a soil chronosequence derived from basalt on Hainan Island, China and its implication for pedogenesis. *Geoderma*, *148*, 206–212.

Hilton, R.G., & West, A.J. (2020). Mountains, erosion and the carbon cycle. *Nature Reviews Earth & Environment*, *1*, 284–299.

Hinckley, D.N. (1962). Variability in 'crystallinity' values among the kaolin deposits of the coastal plain of Georgia and South Carolina. *Clays and Clay Minerals*, *11*, 229–235.

Hong, H.L., Fang, Q., Cheng, L.L., Wang, C.W., & Churchman, G.J. (2016). Microorganism-induced weathering of clay minerals in a hydromorphic soil. *Geochimica et Cosmochimica Acta*, *184*, 272–288.

Hong, H.L., Ji, K.P., Hei, H.T., Wang, C.W., Liu, C., Zhao, L.L., Lanson, B., Zhao, C.L., Fang, Q., & Algeo, T. J. (2023). Clay mineral evolution and formation of intermediate phases during pedogenesis on picrite basalt bedrock under temperate conditions (Yunnan, southwestern China). *Catena*, *220*, 106677.

Hu, X.F., Wei, J., Xu, L.F., Zhang, G.L., & Zhang, W.G. (2009). Magnetic susceptibility of the quaternary Red Clay in subtropical China and its paleoenvironmental implications. *Palaeogeography, Palaeoclimatology, Palaeoecology*, *279*, 216–232.

Huang, K.J., Teng, F.Z., Wei, G.J., Ma, J.L., & Bao, Z.Y. (2012). Adsorption- and desorption-controlled magnesium isotope fractionation during extreme weathering of basalt in Hainan Island, China. *Earth and Planetary Science Letters*, *359–360*, 73–83.

Jiang, K., Qi, H.W., & Hu, R.Z. (2018). Element mobilization and redistribution under extreme tropical weathering of basalts from the Hainan Island, South China. *Journal of Asian Earth Sciences*, *158*, 80–102.

Kardjilov, M.I., Gislason, S.R., & Gisladottir, G. (2006). The effect of gross primary production, net primary production and net ecosystem exchange on the carbon fixation by chemical weathering of basalt in northeastern Iceland. *Journal of Geochemical Exploration*, *88*, 292–295.

Kiczka, M., Wiederhold, J.G., Frommer, J., Voegelin, A., Kraemer, S.M., Bourdon, B., & Kretzschmar, B. (2011). Iron speciation and isotope fractionation during silicate weathering and soil formation in an alpine glacier forefield chronosequence. *Geochimica et Cosmochimica Acta*, *75*, 5559–5573.

Klaes, B., Thiele-Bruhn, S., Woerner, W., Hoeschen, C., Mueller, C.W., Marx, P., Arz, H.W., Breuer, S., & Kilian, R. (2023). Iron (hydr)oxide formation in Andosols under extreme climate conditions. *Scientific Reports*, *13*, article number: 2818.

Krause, A.J., Sluijs, A., van der Ploeg, R., Lenton, T.M., & Pogge von Strandmann, P.A.E. (2023). Enhanced clay formation key in sustaining the Middle Eocene Climatic Optimum. *Nature Geoscience*, *16*, 730–738.

Kovács, J. & Czigány, S. (2017). Soils and weathering. In Richardson, D., Castree, N., Goodchild, M.F., Kobayashi, A., Liu, W., & Marston, R.A. (eds), *The International Encyclopedia of Geography*, doi: 10.1002/9781118786352.wbieg0321. John Wiley & Sons, Ltd.

https://doi.org/10.1017/cmn.2024.14 Published online by Cambridge University Press

Lessovaia, S.N., Plotze, M., Inozemzev, S., & Goryachkin, S. (2016). Traprock transformation into clayey materials in soil environments of the Central Siberian Plateau, Russia. *Clays and Clay Mineral*, *64*, 668–676.

Li, G.J., Hartmann, J., Derry, L.A., West, A.J., You, C.F., Long, X.Y., Zhan, T., Li, L.F., Li., G., Qiu, W.H., Li, T., Liu, L.W., Chen, Y., Ji, J.F., Zhao, L., & Chen, J. (2016). Temperature dependence of basalt weathering. *Earth and Planetary Science Letters*, *443*, 59–69.

Li, M., He, Y., Kang, J., Yang, X., He, Z., Yu, H., & Huang, F. (2017). Why was iron lost without significant isotope fractionation during the lateritic process in tropical environments? *Geoderma*, *290*, 1–9.

Liivamägi, S., Środoń, J., Bojanowski, M.J., Gerdes, A., Stanek, J.J., Williams, L., & Szczerba, M. (2018). Paleosols on the Ediacaran basalts of the East European Craton: a unique record of paleoweathering with minimum diagenetic overprint. *Precambrian Research*, *316*, 66–82.

Lima, A.P.B., Inda, A.V., Zinn, Y.L., & do Nascimento, P.C. (2021). Weathering sequence of soils along a basalt-sandstone toposequence in the Brazilian Cerrado. *Geoderma*, *394*, 115009.

Liu, C.C., Deng, C.L., & Liu, Q.S. (2012). Mineral magnetic studies of the vermiculated red soils in southeast China and their paleoclimatic significance. *Palaeogeography, Palaeoclimatology, Palaeoecology*, *329–330*, 173–183.

Liu, X., Lv, B., Zheng, X.F., Chen, Z.X., & Du, J.H. (2022). Magnetic characteristics of yellow-red soil and transformation of its magnetic minerals in Zhouning, Fujian Province. *Acta Pedologica Sinica*, *59*, 987–998 [Chinese text with English abstract].

Long, X.Y., Ji, J.F., Balsam, Barrón, V., & Torrent, J. (2015). Grain growth and transformation of magnetic particles in red Ferralsols. *Geophysical Research Letters*, *42*, 5762–5770.

Lu, S.G., Xue, Q.F., Zhu, L., & Yu, J.Y. (2008). Mineral magnetic properties of a weathering sequence of soils derived from basalt in Eastern China. *Catena*, *73*, 23–33.

Lyu, H., Watanabe, T., Ota, Y., Hartono, A., Anda, M., Dahlgren, R.A., & Funakawa, S. (2022). Climatic controls on soil clay mineral distributions in humid volcanic regions of Sumatra and Java, Indonesia. *Geoderma*, *425*, 116058.

Ma, J.L., Wei, G.J., Xu, Y.G., Long, W.G., & Sun, W.D. (2007). Mobilization and re-distribution of major and trace elements during extreme weathering of basalt in Hainan Island, South China. *Geochimica et Cosmochimica Acta*, *71*, 3223–3237.

Marques, R., Waerenborgh, J.C., Prudêncio, M.I., Dias, M.I., Rocha, F., & da Silva, E.F. (2014). Iron speciation in volcanic topsoils from Fogo island (Cape Verde) – iron oxide nanoparticles and trace elements concentrations. *Catena*, *113*, 95–106.

Melton, E. D., Swanner, E. D., Behrens, S., Schmidt, C. & Kappler, A. (2014). The interplay of microbially mediated and abiotic reactions in the biogeochemical Fe cycle. *Nature Reviews Microbiology*, *12*, 797–808.

Millet, M.A., Baker, J.A., & Payne, C.E. (2012). Ultra-precise stable Fe isotope measurements by high resolution multiple-collector inductively coupled plasma mass spectrometry with a ^{57}Fe–^{58}Fe double spike. *Chemical Geology*, *304–305*, 18–25.

Nesbitt, H.W., & Young, G.M. (1982). Early proterozoic climates and plate motions inferred from major element chemistry of lutites. *Nature*, *299*, 715–717.

Opfergelt, S., Williams, H.M., Cornelis, J.T., Guicharnaud, R.A., Georg, R.B., Siebert, C., Gislason, S.R., Halliday, A.N., & Burton, K.W. (2017). Iron and silicon isotope behavior accompanying weathering in Icelandic soils, and the implications for iron export from peatlands. *Geochimica et Cosmochimica Acta*, *217*, 273–291.

Orhan, D., & Hüseyin, S. (2018). Effect of toposequences on geochemical mass balance and clay mineral formation in soils developed on basalt parent material under subhumid climate condition. *Indian Journal of Geo-Marine Sciences*, *47*, 1809–1820.

Ouyang, T.P., Tang, Z.H., Zhao, X., Tian, C.J., Ma, J.L., Wei, G.J., Huang, N.S., Li, M.K., & Bian, Y. (2015). Magnetic mineralogy of a weathered tropical basalt, Hainan Island, South China. *Physics of the Earth and Planetary Interiors*, *240*, 105–113.

Perez-Fodich, A., & Derry, L.A. (2019). Organic acids and high soil CO_2 drive intense chemical weathering of Hawaiian basalts: insights from reactive transport models. *Geochimica et Cosmochimica Acta*, *249*, 173–198.

Phillips, J.D., Pawlik, Ł., & Šamonil, P. (2019). Weathering fronts. *Earth-Science Reviews*, *198*, 102925.

Pineau, M., Mathian, M., Baron, F., Rondeau, B., Le Deit, L., Allard, T., & Mangold, N. (2022). Estimating kaolinite crystallinity using near-infrared spectroscopy: implications for its geology on Earth and Mars. *American Mineralogist*, *107*, 1453–1469.

Pizarro, C., Escudey, M., Gacitua, M., & Fabris, J.D. (2017). Iron-bearing minerals from soils developing on volcanic materials from southern Chile. Mineralogical characterization supported by Mössbauer spectroscopy. *Journal of Soil Science and Plant Nutrition*, *17*, 341–365.

Poggere, G.C., Inda, A.V., Barrón, V., Kämpf, N., de Brito, A.D.B., Barbosa, J.Z., & Curi, N. (2018). Maghemite quantification and magnetic signature of Brazilian soils with contrasting parent materials. *Applied Clay Science*, *161*, 385–394.

Pokrovsky, O.S., Schott, J., Kudryavtzev, D.I., & Dupre, B. (2005). Basalt weathering in Central Siberia under permafrost conditions. *Geochimica et Cosmochimica Acta*, *69*, 5659–5680.

Qafoku, N.P., Ranst, E.V., Noble, A., & Baert, G. (2004). Variable charge soils: their mineralogy, chemistry and management. *Advances in Agronomy*, *84*, 159–215.

Qi, M., Gao, T., Wang, Z.R., Liu, Y.H., Xia, Y.F., Song, CS., Liu Y.Z., & Liu, C.S. (2022). Iron solid-phase differentiation controls isotopic fractionation during lateritic weathering of basalt. *Catena*, *217*, 106512.

Rasmussen, C., Dahlgren, R.A., & Southard, R.J. (2010). Basalt weathering and pedogenesis across an environmental gradient in the southern Cascade Range, California, USA. *Geoderma*, *154*, 473–485.

Santos, A.C., da Silva, R.C., da Silva Neto, E.C., dos Anjos, L.H.C., & Perera, M.G. (2021). Weathering and pedogenesis of mafic rock in the Brazilian Atlantic Forest. *Journal of South American Earth Sciences*, *111*, 103452.

Schuth, S., Hurraß, J., Münker, C., & Mansfeldt, T. (2015). Redox-dependent fractionation of iron isotopes in suspensions of a groundwater-influenced soil. *Chemical Geology*, *392*, 74–86.

Sheldon, N.D., & Tabor, N.J. (2009). Quantitative paleoenvironmental and paleoclimatic reconstruction using paleosols. *Earth-Science Reviews*, *95*, 1–52.

Silva, A.C., Bispo, F.H.A., De Souza, S., Ardisson, J.D., Viana, A.J.S., Pereira, M. C., Costa, F.R., Murad, E., & Fabris, J.D. (2013). Iron mineralogy of a grey Oxisol from the Jequitinhonha River Basin, Minas Gerais, Brazil. *Clay Minerals*, *48*, 713–723.

Stucki, J.W. (1988). Structural iron in smectites. In Stucki, J.W., Goodman, B.A., & Schwertmann, D. (eds), *Iron in Soils and Clay Minerals* (pp. 625–675). Reidel Publishing Company, Dordrecht.

Van Breemen, N., & Buurman, P. (2002). The formation of hydromorphic soils. In Van Breemen, N., & Buurman, P. (eds), *Soil Formation* (pp. 159–192). Kluwer Academic Publishers, Dordrecht.

Van Dam, R.L., Harrison, J.B.J., Hirschfeld, D.A., Meglich, T.M., Li, Y.G., & North, R.E. (2008). Mineralogy and magnetic properties of basaltic substrate soils: Kaho'olawe and Big Island, Hawaii. *Soil Science Society of America Journal*, *72*, 244–257.

Vepraskas, M. J., & Faulkner, S. P. (2001) Redox chemistry of hydric soils. In Richardson,J. L., and Vepraskas, M. J. (eds.), *Wetland Soils: Genesis, Hydrology, Landscapes, and Classification* (pp. 85–105). Lewis, New York.

Vilela, E.F., Inda, A.V., & Zinn, Y.L. (2019). Soil genesis, mineralogy and chemical composition in a steatite outcrop under tropical humid climate in Brazil. *Catena*, *183*, 104234.

Vingiani, S., Righi, D., Petit, S., & Terribile, F. (2004). Mixed-layer kaolinite-smectite minerals in a red-black soil sequence from basalt in Sardinia (Italy). *Clays and Clay Minerals*, *52*, 473–483.

Waerenborgh, J.C., Rojas, D.P., Vyshatko, N.P., Shaula, A.L., Kharton, V.V., Marozau, I.P., & Naumovich, E.N. (2003). Fe^{4+} formation in brownmillerite $CaAl_{0.5}Fe_{0.5}O_{2.5+\delta}$. *Materials Letters*, *57*, 4388–4393.

Wang, X.C., Li, Z.X., Li, X.H., Li, J., Liu, Y., Long, W.G., Zhou, J.B., & Wang, F. (2012). Temperature, pressure, and composition of the mantle source region of Late Cenozoic basalts in Hainan Island, SE Asia: a consequence of a young thermal mantle plume close to subduction zones? *Journal of Petrology*, *53*, 177–233.

https://doi.org/10.1017/cmn.2024.14 Published online by Cambridge University Press

Watanabe, T., Ueda, S., Nakao, A., Ze, A.M., Dahlgren, R.A., & Funakawa, S. (2023). Disentangling the pedogenic factors controlling active Al and Fe concentrations in soils of the Cameroon volcanic line. *Geoderma*, *430*, 116289.

White, A.F., & Buss, H.L. (2014). Natural weathering rates of silicate minerals. In Drever, J.I. (ed.), *Treatise on Geochemistry: Surface and Ground Water, Weathering and Soils* (pp. 115–155). Elsevier, Amsterdam.

Wilson, S.G, Lambert, J.J., Nanzyo, M., & Dahlgren, R.A. (2017). Soil genesis and mineralogy across a volcanic lithosequence. *Geoderma*, *285*, 301–312.

Wu, B., Amelung, W., Xing, Y., Bol, R., & Berns, A.E. (2019). Iron cycling and isotope fractionation in terrestrial ecosystems. *Earth-Science Reviews*, *190*, 323–352.

Yang, Z.S., Gao, Z.M., Li, S.R., Luo, T.Y., Li, H.Y., & Rao, W.B. (2001). Characteristics of genetic mineralogy of red-clay type of gold deposit. *Geoscience*, *15*, 216–221 [Chinese text with English abstract].

Yu, G.H., Chi, Z.L., Teng, H.H., Dong, H.L., Kappler, A., Gillings, M.R., Polizzotto, M.L., Liu, C.Q., Zhu, Y.G. (2019). Fungus-initiated catalytic reactions at hyphal-mineral interfaces drive iron redox cycling and biomineralization. *Geochimica et Cosmochimica Acta*, *260*, 192–203.

Yu, X.L., Wang, Y.F., Zhou, G.Z., Peng, G.Y., & Brookes, P.C. (2020). Paleoclimatic fingerprints of ferromanganese nodules in subtropical Chinese soils identified by synchrotron radiation-based microprobes. *Chemical Geology*, *531*, 119357.

Zhu, B.Q., & Wang, H.F. (1989). Nd-Sr-Pb isotopic and chemical evidence for the volcanism with MORB-OIB source characteristics in the Leiqiong area, China. *Geochimica*, *17*, 193–201[Chinese text with English abstract].

Ziegler, K., Hsieh, J.C.C., Chadwick, O.A., Kelly, E.F., Hendricks, D.M., & Savin, S.M. (2003). Halloysite as a kinetically controlled end product of arid-zone basalt weathering. *Chemical Geology*, *202*, 461–478.

https://doi.org/10.1017/cmn.2024.14 Published online by Cambridge University Press